FERMILAB-PUB-11-296-PPD

arXiv:1106.5131v3 [hep-ex] 4 Oct 2011

Measurement of the Cross Section for Prompt Isolated Diphoton Production in $p\bar{p}$ Collisions at $\sqrt{s} = 1.96$ TeV

T. Aaltonen,[21] B. Álvarez González[v],[9] S. Amerio,[41] D. Amidei,[32] A. Anastassov,[36] A. Annovi,[17] J. Antos,[12] G. Apollinari,[15] J.A. Appel,[15] A. Apresyan,[46] T. Arisawa,[56] A. Artikov,[13] J. Asaadi,[51] W. Ashmanskas,[15] B. Auerbach,[59] A. Aurisano,[51] F. Azfar,[40] W. Badgett,[15] A. Barbaro-Galtieri,[26] V.E. Barnes,[46] B.A. Barnett,[23] P. Barria[cc],[44] P. Bartos,[12] M. Bauce[aa],[41] G. Bauer,[30] F. Bedeschi,[44] D. Beecher,[28] S. Behari,[23] G. Bellettini[bb],[44] J. Bellinger,[58] D. Benjamin,[14] A. Beretvas,[15] A. Bhatti,[48] M. Binkley*,[15] D. Bisello[aa],[41] I. Bizjak[gg],[28] K.R. Bland,[5] B. Blumenfeld,[23] A. Bocci,[14] A. Bodek,[47] D. Bortoletto,[46] J. Boudreau,[45] A. Boveia,[11] B. Brau[a],[15] L. Brigliadori[z],[6] A. Brisuda,[12] C. Bromberg,[33] E. Brucken,[21] M. Bucciantonio[bb],[44] J. Budagov,[13] H.S. Budd,[47] S. Budd,[22] K. Burkett,[15] G. Busetto[aa],[41] P. Bussey,[19] A. Buzatu,[31] C. Calancha,[29] S. Camarda,[4] M. Campanelli,[33] M. Campbell,[32] F. Canelli[12],[15] A. Canepa,[43] B. Carls,[22] D. Carlsmith,[58] R. Carosi,[44] S. Carrillo[k],[16] S. Carron,[15] B. Casal,[9] M. Casarsa,[15] A. Castro[z],[6] P. Catastini,[15] D. Cauz,[52] V. Cavaliere[cc],[44] M. Cavalli-Sforza,[4] A. Cerri[f],[26] L. Cerrito[q],[28] Y.C. Chen,[1] M. Chertok,[7] G. Chiarelli,[44] G. Chlachidze,[15] F. Chlebana,[15] K. Cho,[25] D. Chokheli,[13] J.P. Chou,[20] W.H. Chung,[58] Y.S. Chung,[47] C.I. Ciobanu,[42] M.A. Ciocci[cc],[44] A. Clark,[18] G. Compostella[aa],[41] M.E. Convery,[15] J. Conway,[7] M.Corbo,[42] M. Cordelli,[17] C.A. Cox,[7] D.J. Cox,[7] F. Crescioli[bb],[44] C. Cuenca Almenar,[59] J. Cuevas[v],[9] R. Culbertson,[15] D. Dagenhart,[15] N. d'Ascenzo[t],[42] M. Datta,[15] P. de Barbaro,[47] S. De Cecco,[49] G. De Lorenzo,[4] M. Dell'Orso[bb],[44] C. Deluca,[4] L. Demortier,[48] J. Deng[c],[14] M. Deninno,[6] F. Devoto,[21] M. d'Errico[aa],[41] A. Di Canto[bb],[44] B. Di Ruzza,[44] J.R. Dittmann,[5] M. D'Onofrio,[27] S. Donati[bb],[44] P. Dong,[15] M. Dorigo,[52] T. Dorigo,[41] K. Ebina,[56] A. Elagin,[51] A. Eppig,[32] R. Erbacher,[7] D. Errede,[22] S. Errede,[22] N. Ershaidat[y],[42] R. Eusebi,[51] H.C. Fang,[26] S. Farrington,[40] M. Feindt,[24] J.P. Fernandez,[29] C. Ferrazza[dd],[44] R. Field,[16] G. Flanagan[r],[46] R. Forrest,[7] M.J. Frank,[5] M. Franklin,[20] J.C. Freeman,[15] Y. Funakoshi,[56] I. Furic,[16] M. Gallinaro,[48] J. Galyardt,[10] J.E. Garcia,[18] A.F. Garfinkel,[46] P. Garosi[cc],[44] H. Gerberich,[22] E. Gerchtein,[15] S. Giagu[ee],[49] V. Giakoumopoulou,[3] P. Giannetti,[44] K. Gibson,[45] C.M. Ginsburg,[15] N. Giokaris,[3] P. Giromini,[17] M. Giunta,[44] G. Giurgiu,[23] V. Glagolev,[13] D. Glenzinski,[15] M. Gold,[35] D. Goldin,[51] N. Goldschmidt,[16] A. Golossanov,[15] G. Gomez,[9] G. Gomez-Ceballos,[30] M. Goncharov,[30] O. González,[29] I. Gorelov,[35] A.T. Goshaw,[14] K. Goulianos,[48] A. Gresele,[41] S. Grinstein,[4] C. Grosso-Pilcher,[11] R.C. Group,[55] J. Guimaraes da Costa,[20] Z. Gunay-Unalan,[33] C. Haber,[26] S.R. Hahn,[15] E. Halkiadakis,[50] A. Hamaguchi,[39] J.Y. Han,[47] F. Happacher,[17] K. Hara,[53] D. Hare,[50] M. Hare,[54] R.F. Harr,[57] K. Hatakeyama,[5] C. Hays,[40] M. Heck,[24] J. Heinrich,[43] M. Herndon,[58] S. Hewamanage,[5] D. Hidas,[50] A. Hocker,[15] W. Hopkins[g],[15] D. Horn,[24] S. Hou,[1] R.E. Hughes,[37] M. Hurwitz,[11] U. Husemann,[59] N. Hussain,[31] M. Hussein,[33] J. Huston,[33] G. Introzzi,[44] M. Iori[ee],[49] A. Ivanov[o],[7] E. James,[15] D. Jang,[10] B. Jayatilaka,[14] E.J. Jeon,[25] M.K. Jha,[6] S. Jindariani,[15] W. Johnson,[7] M. Jones,[46] K.K. Joo,[25] S.Y. Jun,[10] T.R. Junk,[15] T. Kamon,[51] P.E. Karchin,[57] Y. Kato[n],[39] W. Ketchum,[11] J. Keung,[43] V. Khotilovich,[51] B. Kilminster,[15] D.H. Kim,[25] H.S. Kim,[25] H.W. Kim,[25] J.E. Kim,[25] M.J. Kim,[17] S.B. Kim,[25] S.H. Kim,[53] Y.K. Kim,[11] N. Kimura,[56] M. Kirby,[15] S. Klimenko,[16] K. Kondo,[56] D.J. Kong,[25] J. Konigsberg,[16] A.V. Kotwal,[14] M. Kreps,[24] J. Kroll,[43] D. Krop,[11] N. Krumnack[l],[5] M. Kruse,[14] V. Krutelyov[d],[51] T. Kuhr,[24] M. Kurata,[53] S. Kwang,[11] A.T. Laasanen,[46] S. Lami,[44] S. Lammel,[15] M. Lancaster,[28] R.L. Lander,[7] K. Lannon[u],[37] A. Lath,[50] G. Latino[c],[44] I. Lazzizzera,[41] T. LeCompte,[2] E. Lee,[51] H.S. Lee,[11] J.S. Lee,[25] S.W. Lee[w],[51] S. Leo[bb],[44] S. Leone,[44] J.D. Lewis,[15] C.-J. Lin,[26] J. Linacre,[40] M. Lindgren,[15] E. Lipeles,[43] A. Lister,[18] D.O. Litvintsev,[15] C. Liu,[45] Q. Liu,[46] T. Liu,[15] S. Lockwitz,[59] N.S. Lockyer,[43] A. Loginov,[59] D. Lucchesi[aa],[41] J. Lueck,[24] P. Lujan,[26] P. Lukens,[15] G. Lungu,[48] J. Lys,[26] R. Lysak,[12] R. Madrak,[15] K. Maeshima,[15] K. Makhoul,[30] P. Maksimovic,[23] S. Malik,[48] G. Manca[b],[27] A. Manousakis-Katsikakis,[3] F. Margaroli,[46] C. Marino,[24] M. Martínez,[4] R. Martínez-Ballarín,[29] P. Mastrandrea,[49] M. Mathis,[23] M.E. Mattson,[57] P. Mazzanti,[6] K.S. McFarland,[47] P. McIntyre,[51] R. McNulty[i],[27] A. Mehta,[27] P. Mehtala,[21] A. Menzione,[44] C. Mesropian,[48] T. Miao,[15] D. Mietlicki,[32] A. Mitra,[1] H. Miyake,[53] S. Moed,[20] N. Moggi,[6] M.N. Mondragon[k],[15] C.S. Moon,[25] R. Moore,[15] M.J. Morello,[15] J. Morlock,[24] P. Movilla Fernandez,[15] A. Mukherjee,[15] Th. Muller,[24] P. Murat,[15] M. Mussini[z],[6] J. Nachtman[m],[15] Y. Nagai,[53] J. Naganoma,[56] I. Nakano,[38] A. Napier,[54] J. Nett,[51] C. Neu,[55] M.S. Neubauer,[22] J. Nielsen[e],[26] L. Nodulman,[2] O. Norniella,[22] E. Nurse,[28] L. Oakes,[40] S.H. Oh,[14] Y.D. Oh,[25] I. Oksuzian,[55] T. Okusawa,[39] R. Orava,[21] L. Ortolan,[4] S. Pagan Griso[aa],[41] C. Pagliarone,[52] E. Palencia[f],[9] V. Papadimitriou,[15] A.A. Paramonov,[2] J. Patrick,[15] G. Pauletta[f],[52] M. Paulini,[10] C. Paus,[30] D.E. Pellett,[7] A. Penzo,[52] T.J. Phillips,[14] G. Piacentino,[44] E. Pianori,[43] J. Pilot,[37] K. Pitts,[22] C. Plager,[8] L. Pondrom,[58] K. Potamianos,[46] O. Poukhov*,[13] A. Pranko,[60] F. Prokoshin[x],[13] F. Ptohos[h],[17] E. Pueschel,[10] G. Punzi[bb],[44] J. Pursley,[58] A. Rahaman,[45] V. Ramakrishnan,[58] N. Ranjan,[46] I. Redondo,[29] P. Renton,[40] M. Rescigno,[49] F. Rimondi[z],[6] L. Ristori[44],[15] A. Robson,[19] T. Rodrigo,[9]

T. Rodriguez,[43] E. Rogers,[22] S. Rolli,[54] R. Roser,[15] M. Rossi,[52] F. Rubbo,[15] F. Ruffini[cc],[44] A. Ruiz,[9] J. Russ,[10] V. Rusu,[15] A. Safonov,[51] W.K. Sakumoto,[47] Y. Sakurai,[56] L. Santi[ff],[52] L. Sartori,[44] K. Sato,[53] V. Saveliev[t],[42] A. Savoy-Navarro,[42] P. Schlabach,[15] A. Schmidt,[24] E.E. Schmidt,[15] M.P. Schmidt*,[59] M. Schmitt,[36] T. Schwarz,[7] L. Scodellaro,[9] A. Scribano[cc],[44] F. Scuri,[44] A. Sedov,[46] S. Seidel,[35] Y. Seiya,[39] A. Semenov,[13] F. Sforza[bb],[44] A. Sfyrla,[22] D. Sgalaberna[z], S.Z. Shalhout,[7] T. Shears,[27] P.F. Shepard,[45] M. Shimojima[s],[53] S. Shiraishi,[11] M. Shochet,[11] I. Shreyber,[34] A. Simonenko,[13] P. Sinervo,[31] A. Sissakian*,[13] K. Sliwa,[54] J.R. Smith,[7] F.D. Snider,[15] A. Soha,[15] S. Somalwar,[50] V. Sorin,[4] P. Squillacioti,[15] M. Stancari,[15] M. Stanitzki,[59] R. St. Denis,[19] B. Stelzer,[31] O. Stelzer-Chilton,[31] D. Stentz,[36] J. Strologas,[35] G.L. Strycker,[32] Y. Sudo,[53] A. Sukhanov,[16] I. Suslov,[13] K. Takemasa,[53] Y. Takeuchi,[53] J. Tang,[11] M. Tecchio,[32] P.K. Teng,[1] J. Thom[g],[15] J. Thome,[10] G.A. Thompson,[22] E. Thomson,[43] P. Ttito-Guzmán,[29] S. Tkaczyk,[15] D. Toback,[51] S. Tokar,[12] K. Tollefson,[33] T. Tomura,[53] D. Tonelli,[15] S. Torre,[17] D. Torretta,[15] P. Totaro[ff],[52] M. Trovato[dd],[44] Y. Tu,[43] F. Ukegawa,[53] S. Uozumi,[25] A. Varganov,[32] F. Vázquez[k],[16] G. Velev,[15] C. Vellidis,[3] M. Vidal,[29] I. Vila,[9] R. Vilar,[9] J. Vizán,[9] M. Vogel,[35] G. Volpi[bb],[44] P. Wagner,[43] R.L. Wagner,[15] T. Wakisaka,[39] R. Wallny,[8] S.M. Wang,[1] A. Warburton,[31] D. Waters,[28] M. Weinberger,[51] W.C. Wester III,[15] B. Whitehouse,[54] D. Whiteson[c],[43] A.B. Wicklund,[2] E. Wicklund,[15] S. Wilbur,[11] F. Wick,[24] H.H. Williams,[43] J.S. Wilson,[37] P. Wilson,[15] B.L. Winer,[37] P. Wittich[g],[15] S. Wolbers,[15] H. Wolfe,[37] T. Wright,[32] X. Wu,[18] Z. Wu,[5] K. Yamamoto,[39] J. Yamaoka,[14] T. Yang,[15] U.K. Yang[p],[11] Y.C. Yang,[25] W.-M. Yao,[26] G.P. Yeh,[15] K. Yi[m],[15] J. Yoh,[15] K. Yorita,[56] T. Yoshida[j],[39] G.B. Yu,[14] I. Yu,[25] S.S. Yu,[15] J.C. Yun,[15] A. Zanetti,[52] Y. Zeng,[14] and S. Zucchelli[z6]

(CDF Collaboration†)

[1]*Institute of Physics, Academia Sinica, Taipei, Taiwan 11529, Republic of China*
[2]*Argonne National Laboratory, Argonne, Illinois 60439, USA*
[3]*University of Athens, 157 71 Athens, Greece*
[4]*Institut de Fisica d'Altes Energies, ICREA, Universitat Autonoma de Barcelona, E-08193, Bellaterra (Barcelona), Spain*
[5]*Baylor University, Waco, Texas 76798, USA*
[6]*Istituto Nazionale di Fisica Nucleare Bologna, [z]University of Bologna, I-40127 Bologna, Italy*
[7]*University of California, Davis, Davis, California 95616, USA*
[8]*University of California, Los Angeles, Los Angeles, California 90024, USA*
[9]*Instituto de Fisica de Cantabria, CSIC-University of Cantabria, 39005 Santander, Spain*
[10]*Carnegie Mellon University, Pittsburgh, Pennsylvania 15213, USA*
[11]*Enrico Fermi Institute, University of Chicago, Chicago, Illinois 60637, USA*
[12]*Comenius University, 842 48 Bratislava, Slovakia; Institute of Experimental Physics, 040 01 Kosice, Slovakia*
[13]*Joint Institute for Nuclear Research, RU-141980 Dubna, Russia*
[14]*Duke University, Durham, North Carolina 27708, USA*
[15]*Fermi National Accelerator Laboratory, Batavia, Illinois 60510, USA*
[16]*University of Florida, Gainesville, Florida 32611, USA*
[17]*Laboratori Nazionali di Frascati, Istituto Nazionale di Fisica Nucleare, I-00044 Frascati, Italy*
[18]*University of Geneva, CH-1211 Geneva 4, Switzerland*
[19]*Glasgow University, Glasgow G12 8QQ, United Kingdom*
[20]*Harvard University, Cambridge, Massachusetts 02138, USA*
[21]*Division of High Energy Physics, Department of Physics, University of Helsinki and Helsinki Institute of Physics, FIN-00014, Helsinki, Finland*
[22]*University of Illinois, Urbana, Illinois 61801, USA*
[23]*The Johns Hopkins University, Baltimore, Maryland 21218, USA*
[24]*Institut für Experimentelle Kernphysik, Karlsruhe Institute of Technology, D-76131 Karlsruhe, Germany*
[25]*Center for High Energy Physics: Kyungpook National University, Daegu 702-701, Korea; Seoul National University, Seoul 151-742, Korea; Sungkyunkwan University, Suwon 440-746, Korea; Korea Institute of Science and Technology Information, Daejeon 305-806, Korea; Chonnam National University, Gwangju 500-757, Korea; Chonbuk National University, Jeonju 561-756, Korea*
[26]*Ernest Orlando Lawrence Berkeley National Laboratory, Berkeley, California 94720, USA*
[27]*University of Liverpool, Liverpool L69 7ZE, United Kingdom*
[28]*University College London, London WC1E 6BT, United Kingdom*
[29]*Centro de Investigaciones Energeticas Medioambientales y Tecnologicas, E-28040 Madrid, Spain*
[30]*Massachusetts Institute of Technology, Cambridge, Massachusetts 02139, USA*
[31]*Institute of Particle Physics: McGill University, Montréal, Québec, Canada H3A 2T8; Simon Fraser University, Burnaby, British Columbia, Canada V5A 1S6; University of Toronto, Toronto, Ontario, Canada M5S 1A7; and TRIUMF, Vancouver, British Columbia, Canada V6T 2A3*
[32]*University of Michigan, Ann Arbor, Michigan 48109, USA*

[33]Michigan State University, East Lansing, Michigan 48824, USA
[34]Institution for Theoretical and Experimental Physics, ITEP, Moscow 117259, Russia
[35]University of New Mexico, Albuquerque, New Mexico 87131, USA
[36]Northwestern University, Evanston, Illinois 60208, USA
[37]The Ohio State University, Columbus, Ohio 43210, USA
[38]Okayama University, Okayama 700-8530, Japan
[39]Osaka City University, Osaka 588, Japan
[40]University of Oxford, Oxford OX1 3RH, United Kingdom
[41]Istituto Nazionale di Fisica Nucleare, Sezione di Padova-Trento, [aa]University of Padova, I-35131 Padova, Italy
[42]LPNHE, Universite Pierre et Marie Curie/IN2P3-CNRS, UMR7585, Paris, F-75252 France
[43]University of Pennsylvania, Philadelphia, Pennsylvania 19104, USA
[44]Istituto Nazionale di Fisica Nucleare Pisa, [bb]University of Pisa,
[cc]University of Siena and [dd]Scuola Normale Superiore, I-56127 Pisa, Italy
[45]University of Pittsburgh, Pittsburgh, Pennsylvania 15260, USA
[46]Purdue University, West Lafayette, Indiana 47907, USA
[47]University of Rochester, Rochester, New York 14627, USA
[48]The Rockefeller University, New York, New York 10065, USA
[49]Istituto Nazionale di Fisica Nucleare, Sezione di Roma 1,
[ee]Sapienza Università di Roma, I-00185 Roma, Italy
[50]Rutgers University, Piscataway, New Jersey 08855, USA
[51]Texas A&M University, College Station, Texas 77843, USA
[52]Istituto Nazionale di Fisica Nucleare Trieste/Udine,
I-34100 Trieste, [ff]University of Trieste/Udine, I-33100 Udine, Italy
[53]University of Tsukuba, Tsukuba, Ibaraki 305, Japan
[54]Tufts University, Medford, Massachusetts 02155, USA
[55]University of Virginia, Charlottesville, VA 22906, USA
[56]Waseda University, Tokyo 169, Japan
[57]Wayne State University, Detroit, Michigan 48201, USA
[58]University of Wisconsin, Madison, Wisconsin 53706, USA
[59]Yale University, New Haven, Connecticut 06520, USA
[60]Ernest Orlando Lawrence Berkeley National Laboratory, Berkeley, California 9472 0, USA

(Dated: March 8, 2013)

This article reports a measurement of the production cross section of prompt isolated photon pairs in proton-antiproton collisions at $\sqrt{s} = 1.96$ TeV using the CDF II detector at the Fermilab Tevatron collider. The data correspond to an integrated luminosity of 5.36 fb^{-1}. The cross section is presented as a function of kinematic variables sensitive to the reaction mechanisms. The results are compared with three perturbative QCD calculations: (1) a leading order parton shower Monte Carlo, (2) a fixed next-to-leading order calculation and (3) a next-to-leading order/next-to-next-to-leading-log resummed calculation. The comparisons show that, within their known limitations, all calculations predict the main features of the data, but no calculation adequately describes all aspects of the data.

I. INTRODUCTION

The measurement of the production cross section of two energetic isolated central photons (diphotons) in high energy hadron collisions is important for testing standard model (SM) predictions in the domain of searches for undiscovered particles and new physics. Understanding the reaction mechanisms in the complicated environment formed in such collisions is a challenge for perturbative Quantum ChromoDynamics (pQCD) calculations. Pho-

*Deceased
†With visitors from [a]University of Massachusetts Amherst, Amherst, Massachusetts 01003, [b]Istituto Nazionale di Fisica Nucleare, Sezione di Cagliari, 09042 Monserrato (Cagliari), Italy, [c]University of California Irvine, Irvine, CA 92697, [d]University of California Santa Barbara, Santa Barbara, CA 93106 [e]University of California Santa Cruz, Santa Cruz, CA 95064, [f]CERN,CH-1211 Geneva, Switzerland, [g]Cornell University, Ithaca, NY 14853, [h]University of Cyprus, Nicosia CY-1678, Cyprus, [i]University College Dublin, Dublin 4, Ireland, [j]University of Fukui, Fukui City, Fukui Prefecture, Japan 910-0017, [k]Universidad Iberoamericana, Mexico D.F., Mexico, [l]Iowa State University, Ames, IA 50011, [m]University of Iowa, Iowa City, IA 52242, [n]Kinki University, Higashi-Osaka City, Japan 577-8502, [o]Kansas State University, Manhattan, KS 66506, [p]University of Manchester, Manchester M13 9PL, England, [q]Queen Mary, University of London, London, E1 4NS, England, [r]Muons, Inc., Batavia, IL 60510, [s]Nagasaki Institute of Applied Science, Nagasaki, Japan, [t]National Research Nuclear University, Moscow, Russia, [u]University of Notre Dame, Notre Dame, IN 46556, [v]Universidad de Oviedo, E-33007 Oviedo, Spain, [w]Texas Tech University, Lubbock, TX 79609, [x]Universidad Tecnica Federico Santa Maria, 110v Valparaiso, Chile, [y]Yarmouk University, Irbid 211-63, Jordan, [gg]On leave from J. Stefan Institute, Ljubljana, Slovenia.

tons orginating from hard collisions of hadrons ("direct" or "prompt" photons) are an ideal probe for testing these calculations because they do not interact with other final state particles, and their energies and directions can be measured with high precision in modern electromagnetic calorimeters. Prompt diphoton production creates an irreducible background to the diphoton decay channel of proposed new particles, such as low mass Higgs bosons or Randall-Sundrum gravitons in models of extra spatial dimensions [1, 2]. An improved knowledge of the SM background will help the development of more powerful search strategies for these particles.

The basic mechanisms of prompt diphoton production in hadron collisions are quark-antiquark annihilation $q\bar{q} \to \gamma\gamma$, quark-gluon scattering $gq \to \gamma\gamma q$, and gluon-gluon fusion $gg \to \gamma\gamma$. The respective basic diagrams are shown in Fig. 1. At the Tevatron, the dominant mechanism is quark-antiquark annihilation. In quark-gluon scattering, most of the time at least one of the two photons is emitted almost parallel to the scattered quark. Contributions from this mechanism are therefore suppressed by requiring isolated prompt photons. Each mechanism can be modeled by calculating the respective matrix element for the specific event kinematics. Matrix element calculations of Leading Order (LO) in the strong coupling are relatively simple and are thus implemented in advanced parton shower Monte Carlo (MC) event generators [3–5], which allow for gluon and photon radiation as well as multiple interactions in the colliding beams. By including radiation before and after the hard scattering, parton shower generators take into account soft gluon and photon emissions, thus resulting in an effective resummation of all of the Leading Logarithmic (LL) terms in the cross section to all orders of the strong and electromagnetic couplings constants. Next-to-Leading Order (NLO) calculations [6–8] additionally include one-loop corrections at the cost of not featuring realistic multi-particle event representations as the LO generators do. Recent NLO calculations include an analytical resummation of the cross section for initial-state gluon radiation to all orders in the strong coupling constant [8], reaching a higher logarithmic accuracy than in the parton shower Monte Carlo generators. By this method, all soft gluon emissions in the initial state are taken into account, and reliable predictions for the low diphoton transverse momentum region are possible. A fixed-order NLO calculation implemented by the DIPHOX program [6] also accounts for the case where a final state quark loses almost all of its energy to the photon detected in the event [9]. This process is called "fragmentation" and, in contrast to final state photon radiation in parton showering, it involves non-perturbative calculations. One or both photons in the event may come from fragmentation. The case where both photons come from fragmentation of a single quark is also possible, but is not included in calculations, as in this case the photons are nearly collinear and non-isolated most of the time.

The prompt diphoton cross section has been previously measured by the CDF Collaboration using 200 pb^{-1} of data [10], but the large statistical uncertainties did not allow for a precise comparison with theoretical calculations. The nearly 30–times larger CDF II data set currently available presents an opportunity to significantly extend the kinematic range and perform a detailed study of diphoton kinematic distributions. A recent measurement of the diphoton cross section using 4.2 fb^{-1} has been reported by the D0 Collaboration [11]. The reported differential cross sections were only partly reproduced by theoretical calculations [3, 6, 8], although the discrepancies between the NLO calculations [6, 8] and the data were less important in kinematic regions where the Higgs boson or new heavy particles are expected.

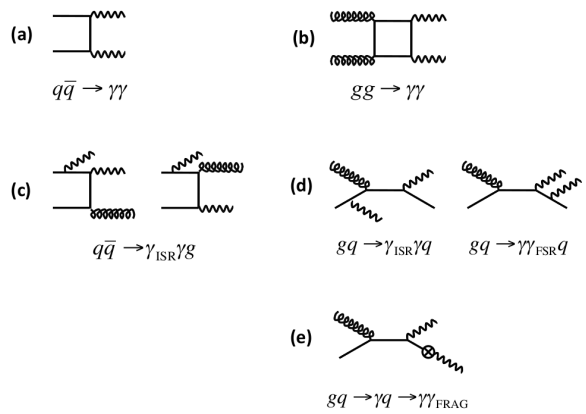

FIG. 1: Basic diagrams for prompt diphoton production: (a-b) direct, (c-d) one-photon radiation from an initial- (ISR) or final-state quark (FSR), (e) fragmentation where one photon is emitted along the direction of a final-state quark taking almost all of its energy. The symbol $\otimes$ denotes the non-perturbative mechanism of the fragmentation process (FRAG).

This article is organized as follows. An overview of the detector is given in Section II. The event selection is presented in Section III. Section IV deals with extracting the cross section from the selected diphoton sample. The results are presented and discussed in Section V. The conclusions are given in Section VI. Appendix A explains details of the non-prompt photon subtraction technique introduced in Section IV. Finally, tables of the measured cross section, differential in various kinematic quantities, are given in Appendix B.

II. DETECTOR OVERVIEW

The CDF II detector is a cylindrically–symmetric apparatus [12] designed to study $p\bar{p}$ collisions at the Fermilab Tevatron. The detector has been described in detail elsewhere [13]; only the detector components that are

relevant to this analysis are briefly discussed here. The magnetic spectrometer consists of tracking devices inside a 3-m diameter, 5-m long superconducting solenoid magnet which provides an axial magnetic field of 1.4 T. A set of silicon microstrip detectors (L00, SVX, and ISL) [14–16] and a 3.1-m long drift chamber (COT) [17] with 96 layers of sense wires measure momenta and trajectories (tracks) of charged particles in the pseudorapidity regions of $|\eta|<2$ and $|\eta|<1$ [12], respectively. Surrounding the magnet coil is the projective-tower-geometry sampling calorimeter, which is used to identify and measure the energy and direction of photons, electrons, and jets. The calorimeter consists of lead-scintillator electromagnetic and iron-scintillator hadron compartments and it is divided into a central barrel ($|\eta|<1.1$) and a pair of "end plugs" that cover the region $1.1<|\eta|<3.6$. The central calorimeter is composed of towers with a segmentation of $\Delta\eta \times \Delta\phi \simeq 0.1 \times 15^o$. The energy resolution of the central electromagnetic calorimeter for electrons is $\sigma(E_{\rm T})/E_{\rm T} = 13.5\%/\sqrt{E_{\rm T}({\rm GeV})} \oplus 1.5\%$ [18], while the energy resolution of the central hadron calorimeter for charged pions that do not interact in the electromagnetic section is $\sigma(E_{\rm T})/E_{\rm T} = 50\%/\sqrt{E_{\rm T}({\rm GeV})} \oplus 3\%$ [19]. Multiwire proportional chambers with cathode-strip readout (the CES system), located at the depth of six radiation lengths (near shower maximum) in the central electromagnetic calorimeter, are used for identification and precise position measurement of photons and electrons. Cathode strips and anode wires, with a channel spacing between 1.5 cm and 2 cm, running along the azimuthal (strips) and the beam line (wires) direction provide location and two-dimensional profiles of electromagnetic showers. The position resolution of the CES is 2 mm for a 50 GeV photon. The electromagnetic compartments of the calorimeter are also used to measure the arrival time of particles depositing energy in each tower [20]. A system of Cherenkov luminosity counters (CLC) [21], located around the beam pipe and inside the plug calorimeters, is used to measure the number of inelastic $p\bar{p}$ collisions per bunch crossing, and thereby the luminosity.

The online event selection at CDF is done by a three-level trigger [22] system with each level providing a rate reduction sufficient to allow for processing at the next level with minimal deadtime. Level-1 uses custom–designed hardware to find physics objects based on a subset of the detector information. Level-2 does limited event reconstruction. Level-3 uses the full detector information and consists of a farm of computers that reconstruct the data and apply selection criteria similar to the offline requirements.

III. DATA SELECTION AND EVENT RECONSTRUCTION

Inclusive $\gamma\gamma$ events are selected online by a three-level trigger that requires two isolated electromagnetic (EM) clusters with $E_{\rm T}^{\gamma}>12$ GeV (diphoton-12 trigger) or two electromagnetic clusters with $E_{\rm T}^{\gamma}>18$ GeV and no isolation requirement (diphoton-18 trigger). The transverse energy of the clusters is calculated with respect to the nominal center of the detector at z=0 cm. The trigger requirements at each level are briefly described below.

At Level-1, events having two towers with EM $E_{\rm T}>8$ GeV each are required. For each trigger tower, the amount of energy in the hadronic compartment of the calorimeter (E^{HAD}) has to be consistent with that of an electromagnetic object. A trigger tower consists of two adjacent towers in the same calorimeter wedge, so that the granularity is approximately $\Delta\eta \times \Delta\phi \simeq 0.2 \times 15^o$.

The Level-2 requirements are different for the two triggers. The diphoton-12 trigger selects events if there are two isolated seeds with EM $E_{\rm T}>10$ GeV each. The isolation (ISO) energy is calculated as a sum of the transverse energy in the towers nearby the seed tower. The ISO energy for both photons has to be less than 3 GeV or 15% of the seed energy, whatever is larger. The diphoton-18 trigger requires two towers with EM $E_{\rm T}>16$ GeV each at Level-2.

Events are fully reconstructed at Level-3. At this level, for all photons in both triggers, the energy profile at the shower maximum of each photon candidate has to be consistent with that of a single photon. The diphoton-12 trigger selects events with two isolated photon candidates with $E_{\rm T}>12$ GeV. The isolation energy at level-3 is calculated as the sum of $E_{\rm T}$ in all towers (except for photon towers) within the cone of $\Delta R = \sqrt{(\Delta\eta)^2 + (\Delta\phi)^2} < 0.4$ centered around the photon candidate. This ISO energy has to be less than 2 GeV or 10% of the photon energy, whatever is larger. The diphoton-18 trigger has no isolation requirement and accepts events with two photon candidates with $E_{\rm T}>18$ GeV. Table I gives a summary of all trigger requirements for events with EM objects in the central calorimeter and with $E_{\rm T}$ calculatated with respect to the event vertex.

The triggered $\gamma\gamma$ candidate events are then subject to the offline selection. Each event is required to have two central photon candidates inside a well-instrumented region of the calorimeter (approximately $0.05<|\eta|<1.05$) with $E_{\rm T}>17$ GeV for one candidate and $E_{\rm T}>15$ GeV for the other. This asymmetric cut helps to avoid instabilities in fixed NLO calculations [6]. Photon candidates must satisfy strict (referred to as "tight") photon identification requirements. The EM cluster has to be located inside the well–instrumented region of the CES chamber, away from the ϕ-boundary of a calorimeter tower [23]. The energy deposition pattern in both transverse profiles at CES has to be consistent with that of a single electromagnetic object. The ratio of the energy measured in the hadron (HAD) calorimeter to the EM energy, $E^{\rm HAD}/E^{\rm EM}$, has to satisfy the requirement $E^{HAD}/E^{EM}<0.055+0.00045\times E^{\gamma}$. To distinguish photons from electrons, no high-$p_{\rm T}$ charged–particle track should point into the cluster ($N_{track}\leq 1$ with track $p_{\rm T}<1.0+0.005\times E_{\rm T}$). The main sources of

TABLE I: Summary of the diphoton trigger requirements.

Trigger Level	Diphoton-12	Diphoton-18
Level-1	EM $E_{\rm T} > 8$ GeV	same
	$E^{HAD}/E^{EM} < 0.125$	same
	$N_{cluster} = 2$	same
Level-2	EM $E_{\rm T} > 10$ GeV	EM $E_{\rm T} > 16$ GeV
	$E^{HAD}/E^{EM} < 0.125$	same
	$E_{\rm T}^{ISO} < 3$ GeV or $E_{\rm T}^{ISO}/E_{\rm T} < 0.15$	not applied
	$N_{cluster} = 2$	same
Level-3	EM $E_{\rm T} > 12$ GeV	EM $E_{\rm T} > 18$ GeV
	$E^{HAD}/E^{EM} < 0.055 + 0.00045\times E/\text{GeV}$ if $E < 200$ GeV	same
	$E_{\rm T}^{ISO} < 2$ GeV or $E_{\rm T}^{ISO}/E_{\rm T} < 0.1$	not applied
	shower profile: $\chi^2_{CES} < 20$	same
	$N_{cluster} = 2$	same

"fake" photons are energetic π^0 and η^0 mesons produced in jets. These mesons are usually produced in association with other particles. To reduce this contamination from jets, the photon candidate must be isolated in the calorimeter. To calculate the calorimeter isolation (cal-ISO), the $E_{\rm T}$ deposited in the calorimeter towers within the cone of $\Delta R < 0.4$ around the EM cluster is summed, and the $E_{\rm T}$ of the EM cluster is subtracted. Cal-ISO is then corrected for the photon's energy leakage into towers in the neighboring wedge and for the contribution from multiple interactions in the same bunch crossing [24]. Cal-ISO must be consistent with the amount of energy expected from the underlying event (see Table II). In addition to the calorimeter isolation, there should be no other significant energy ($E_{\rm T}$ of 2nd CES cluster) deposited in the CES chamber containing the photon candidate. Table II provides a summary of the photon identification requirements described above. To reduce contamination due to cosmic-ray, beam-related, and other non-collision backgrounds, the event must contain a well-reconstructed vertex, formed from tracks, with $|z|<60$ cm. If multiple vertices are reconstructed, the vertex with the largest$\sum p_{\rm T}$ of the associated tracks is selected. The transverse energy of the photon candidates is calculated with respect to this primary vertex.

Inclusive $\gamma\gamma$ events satisfying the above criteria form the baseline $\gamma\gamma$ sample used in the analysis. Due to the presence of fakes, this sample consists of real $\gamma\gamma$, *jet*-γ and *jet-jet* events. (An object misidentified as a photon is referred to as a "fake" photon.) Events with one or two fake photons are classified as background. The baseline signal plus background $\gamma\gamma$ sample consists of roughly 60,000 events in data corresponding to 5.36 fb^{-1} of integrated luminosity. Signal and background samples were simulated with the PYTHIA event generator which includes simulation of the underlying event and multiple hadron interactions, as well as initial- (ISR) and final-state radiation (FSR) and a hadronization model of the final state partons [3]. The PYTHIA events were processed through a GEANT-based detector simulation [25] and trigger emulation, followed by the same reconstruction program as that for the data.

IV. CROSS SECTION MEASUREMENT

This section describes the steps of the cross section measurement. Kinematic variables of interest are histogrammed to measure the corresponding differential cross section. The background is subtracted from each histogram bin. The signal histograms are normalized to the integrated luminosity and to the size of each bin to obtain uncorrected differential cross section histograms. These are then corrected for the reconstruction efficiency, acceptance, and resolution effects.

A. Background Subtraction

The fake photon background subtraction is based on the use of the track isolation (track-ISO), which is calculated as the $\sum p_{\rm T}$ of tracks with ΔR to the photon <0.4 and $|z_{vertex}$-$z_{track}|<5$ cm. The concept of this technique is similar to the one used in the earlier measurement of the inclusive photon cross section [10]. The main idea behind the method is that true and fake photons have very different isolation distributions (see Fig. 2). Therefore, one expects different efficiencies for signal (true photons) and background (fake photons) for a given isolation cut. In a single-photon sample this property can be used to extract the number of true photons:

$$w = \sum_{i=1}^{N} \frac{\epsilon_i - \epsilon_b(E_{{\rm T}i})}{\epsilon_s(E_{{\rm T}i}) - \epsilon_b(E_{{\rm T}i})} \quad (1)$$

where ϵ_i=1 if track-ISO<*cut* and ϵ_i=0 if track-ISO>*cut*, $\epsilon_s(E_{\rm T})$ is the signal efficiency for track-ISO<*cut*, $\epsilon_b(E_{\rm T})$ is the background efficiency for track-ISO<*cut* and N is the total number of candidate photons in the sample. This technique can be generalized in the case of the $\gamma\gamma$

TABLE II: Summary of the standard ("tight") photon identification requirements for the $\gamma\gamma$ sample.

Cuts	"Tight" photon ID
Calorimeter fiduciality	central
$E_{\rm T}^{\gamma}$	$\geq$ 15 GeV ($1^{\rm st}\gamma$), $\geq$ 17 GeV ($2^{\rm nd}\gamma$)
Shower profile in CES: χ^2	$\leq$20
E^{HAD}/E^{EM}	$\leq$0.055+0.00045$\times E$/GeV
cal-ISO	$\leq$0.1$\times E_{\rm T}$ if $E_{\rm T}$<20 GeV or $\leq$2.0 GeV+0.02$\times$($E_{\rm T}$ − 20 GeV)
N_{tracks} in cluster	$\leq$ 1
track $p_{\rm T}$ if $N_{tracks} = 1$	$\leq$1.0 GeV+0.005$\times E_{\rm T}$
$E_{\rm T}$ of 2nd CES cluster	$\leq$0.14$\times E_{\rm T}$ if $E_{\rm T}$<18 GeV $\leq$2.4 GeV+0.01$\times E_{\rm T}$ if $E_{\rm T}\geq$18 GeV

sample and is based on a maximum likelihood approach which is described in detail in Appendix A.

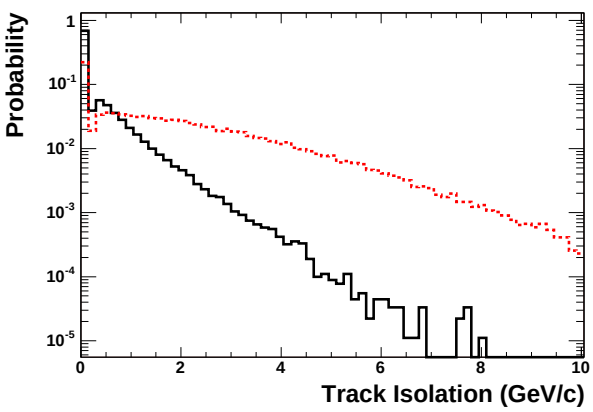

FIG. 2: The track-ISO distribution in signal (black–solid) and background (red–dashed) events.

As mentioned in Section III, two types of isolation can be defined for central photons: calorimeter and track isolation. Cal-ISO is sensitive to the following contributions: underlying event (UE), multiple interactions (MI), leakage from the photon cluster (LE), and fragmentation contribution (FR) from jets (for fakes). Track-ISO, on the other hand, is only a measure of UE and FR. Therefore, it can potentially offer a better separation between true and fake photons. Using track-ISO for the fake photon background subtraction also has additional advantages that low-$P_{\rm T}$ tracks are very well measured (unlike the calorimeter energy) and jet fragmentation studies [26] indicate that track observables are well described by PYTHIA both for the UE and for the jets.

To perform the background subtraction, signal (ϵ_s) and background (ϵ_b) efficiencies are needed for a certain cut on track-ISO. The form of Eq. 1 suggests that the best accuracy in photon purity can be achieved when the absolute value of the denominator is maximum. When this happens the terms in the sum of Eq. 1 are minimized in magnitude and thus the purity is less sensitive to the statistical uncertainty of the number of events in the sample. Therefore, a scan of $\epsilon_s - \epsilon_b$ as a function of the track-ISO cut is performed using MC samples of true and fake photons. The difference peaks at track-ISO$\sim$1 GeV. The threshold of the track-ISO cut for the signal and background efficiency functions is thus chosen at 1 GeV.

The signal track-ISO efficiency is obtained from PYTHIA photon–plus–jet samples. The background efficiency is obtained from PYTHIA dijet samples. All PYTHIA samples used in this work are derived from version 6.2.16 of the program using the CTEQ5L PDF set for [27] and the "tune A" for UE parameters [28]. Background events are filtered out if a detector photon is matched to a generator level photon originating from quark ISR or FSR. This ensures that the background track-ISO efficiency function is obtained for neutral hadrons (mostly π^0 or η^0) faking a photon signature. Similarly, for the signal events detector photons are required to match generator level photons from the hard scattering (thus fragmentation photons are removed). The signal efficiency ϵ_s and the background efficiency ϵ_b are shown in Fig. 3 as functions of the photon $E_{\rm T}$. Both functions are parameterized by a linear combination of an exponential and a constant.

The isolation cones for the two photon candidates are not entirely independent. For example, if a particular event has a higher (lower) than average underlying event activity, then it is likely that both isolation cones will simultaneously have more (less) energy. In addition, the ordering in $E_{\rm T}$ of the two photons also introduces some bias. The signal (for $E_{\rm T}$<50 GeV) and the background track-ISO efficiencies drop with increasing $E_{\rm T}$ (see Fig. 3). Therefore, the lower $E_{\rm T}$ threshold for the first photon in the event relative to the second photon implies, on average, that the $E_{\rm T}$ of the first photon will be systematically lower than the $E_{\rm T}$ of the second photon, thus introducing some bias due to the $E_{\rm T}$ dependence of the efficiencies. This effect is negligible for $E_{\rm T}$>50 GeV, where the signal track-ISO efficiency is flat and the background is weak, but it becomes significant at low $E_{\rm T}$. It is a small effect in the single photon purity, but it is at least a factor of two more important for diphoton events. These cor-

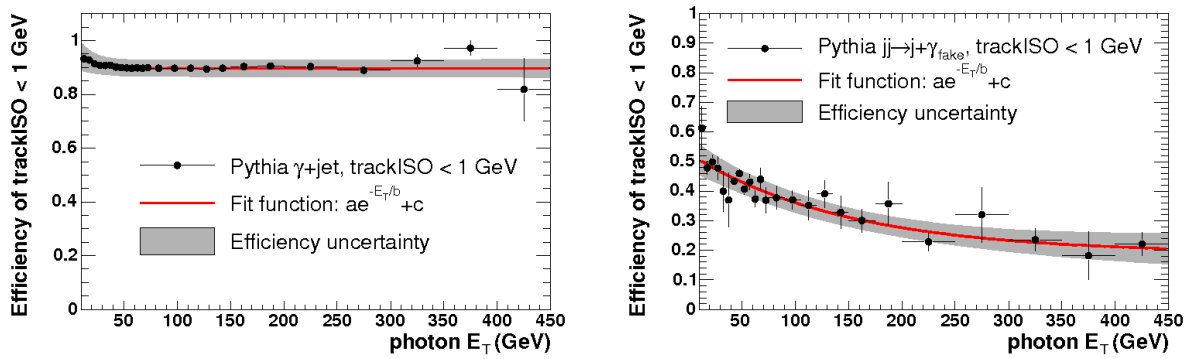

FIG. 3: Signal (left) and background (right) efficiencies for track-ISO<1 GeV. The shaded area is the total systematic uncertainty.

relations must be taken into account when calculating a probability of two photon candidates to pass-pass, pass-fail, fail-pass or fail-fail the 1 GeV isolation cut described above. PYTHIA diphoton events were used to obtain "per event" track-ISO efficiencies for these combinations. Correlations are much less important for events with one or two fake photons because they are diluted by a much larger contribution from jet fragmentation.

The systematic uncertainties in the signal and background track-ISO efficiencies are estimated and propagated into the final estimate of photon purity. Correlations between different sources of systematics are taken into account. The following sources of uncertainties are considered: 1) mis-modeling of the distribution of the number of vertices (N_{vx}) in MC (pile-up effect); 2) statistical uncertainties in the fit parameters; 3) choice of the fit function for the efficiency; 4) generator–related data-MC differences; 5) effect of the $E_{\rm T}$ threshold for selected photon candidates (only for the background). These uncertainties are presented in Fig. 4 and discussed below.

The MC simulation does not describe accurately the distribution of the number of reconstructed vertices. This effect can be either removed by re-weighting the MC to match the data or the associated uncertainty can be assigned for the effect of mis-modeling. The latter approach is chosen in this analysis because the track-ISO, to leading order, is not sensitive to the presence of multiple interactions and the effect is very small. This uncertainty is conservatively estimated as the difference between the extreme cases of track-ISO efficiencies obtained in events with N_{vx}=1 and track-ISO efficiencies obtained in events with N_{vx}>1. For the photon energies relevant to this analysis, the relative effect is <1% for the signal and <3% for the background.

The fit statistical uncertainties are included in the estimation of systematic uncertainties. Correlations between fit parameters are properly taken into account. The relative effect is negligible for the signal and 1%-3% for the background in the range of photon energies relevant to this analysis.

The default fit function choice is an exponential plus a constant term. As one can see from the track-ISO efficiency plots shown in Fig. 3, the quality of the fit is very good. The studies of the efficiency dependence on the track-ISO cut indicated that, for some cut values, the exponential plus a linear function can be a better fit to the signal efficiency. This function was thus chosen as an alternative track-ISO efficiency parameterization and the difference with the default function was taken as the associated uncertainty. The relative effect is <1% for both signal and background with $E_{\rm T}$<200 GeV.

The modeling of both signal and background relies on the MC. Therefore, it is necessary to assign a systematic uncertainty on possible data-MC differences both for signal and background photons. In the case of signal, it is necessary to check the modeling of the underlying event in the MC. This is done by means of complementary cones. The complementary cones are chosen such that their axes have the same angle θ with respect to the beam line as the photon candidate and are rotated by $\pm\pi/2$ in ϕ. These cones are assumed, on average, to collect the same amount of the underlying event as cones of the same size around true photons. This assumption is tested and confirmed in the MC. It is also checked that complementary cones for signal and background look very similar. Finally, the signal track-ISO efficiency is obtained from complementary cones in data and signal MC and the difference between the two is taken as the associated systematic uncertainty in the signal track-ISO efficiency. The comparison of track-ISO efficiencies for complementary cones in data, MC signal and background is shown in Fig. 5. The relative effect is ∼3.5% for most of the photon energies. This is the largest systematic uncertainty for the signal track-ISO efficiency. The systematic uncertainty from this source decreases from 5.5% at $E_{\rm T}$=10 GeV to ∼3.5% at $E_{\rm T}$=40 GeV and then it stays at roughly the same level for $E_{\rm T}$>40 GeV. An additional uncertainty arises from the fact that the signal efficiency is derived from true photons generated only by direct $gq \to \gamma q$, $q\bar{q} \to \gamma g$ and $gg \to \gamma g$ production, omitting photons radiated from initial or final state quarks. Fig. 6 shows that the track isolation of photons radiated from

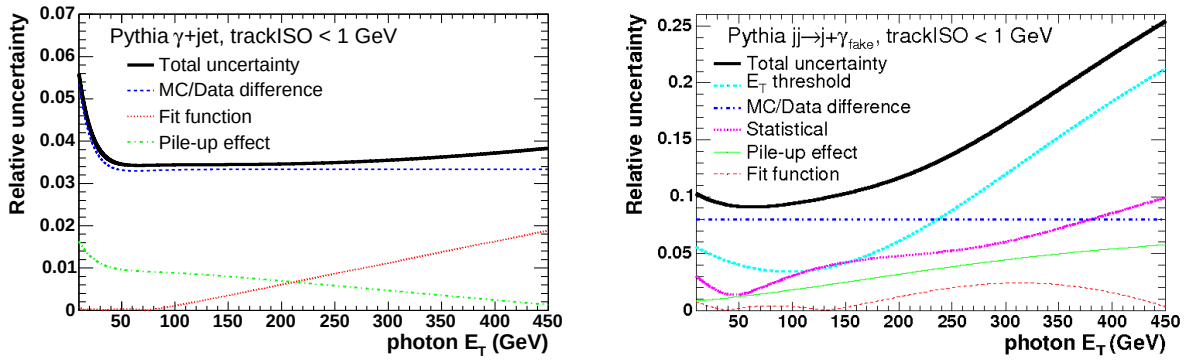

FIG. 4: Relative systematic uncertainties on the signal (left) and background (right) efficiencies for track-ISO<1 GeV.

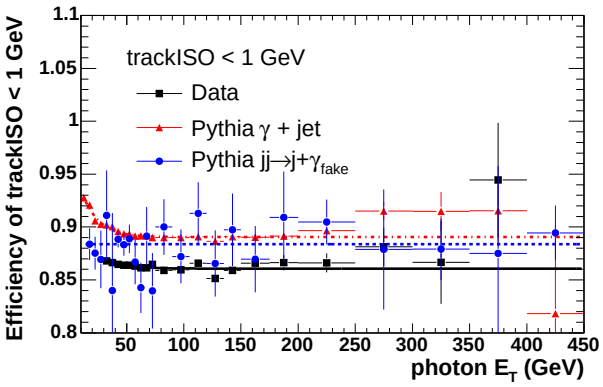

FIG. 5: Comparison of track-ISO<1 GeV efficiencies in complementary cones from data (squares), signal MC (triangles) and background MC (circles).

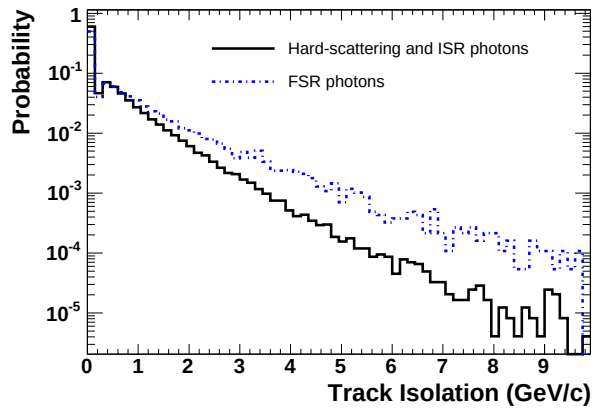

FIG. 6: The track-ISO distribution in hard scattering and ISR (blue) and FSR (black) events.

final state quarks is somewhat different than that of photons produced by hard scattering or radiated from initial state quarks. This difference is estimated to have a constant 2% effect on the signal track-ISO efficiency which is added to its total systematic uncertainty.

The systematic uncertainty due to data-MC differences in the track-ISO background efficiency is estimated by comparing the track-ISO cut efficiency for a leading track in dijet events from data and MC. This method assumes that jets with a leading neutral particle (e.g., π^0/η) have the same or very similar fragmentation properties as jets with a leading charged particle (e.g., $\pi^{\pm}$ or $K^{\pm}$). The following procedure is applied to both data and MC. Events with two well-balanced and back-to-back jets are used, satisfying $|E_{\rm T}(\text{jet1})-E_{\rm T}(\text{jet2})|/[E_{\rm T}(\text{jet1})+E_{\rm T}(\text{jet2})]<0.3$ and $|\phi(\text{jet1})-\phi(\text{jet2})|>2.7$ rad. The event is rejected if there is a third jet with $E_{\rm T}>0.1\times[E_{\rm T}(\text{jet1})+E_{\rm T}(\text{jet2})]$. One of the jets (a probe jet) is required to be in the central detector region, $|\eta|<1.1$, thus matching the pseudorapidity requirement for photons. In the next step, a well-reconstructed track (a probe track) is selected with the largest $p_{\rm T}$ inside the probe jet, i.e. inside a cone of ΔR=0.4 around the jet direction. For this track, an analog of the cal-ISO is calculated as the $\sum E_{\rm T}$ of all towers inside a cone of ΔR=0.4 around the track direction. Towers associated with the track (up to 3 towers in η) are excluded from the sum. The cal-ISO for the probe track has to satisfy exactly the same requirements as the isolation for a photon with $E_{\rm T}$=$p_{\rm T}$. An analog of the track-ISO for the probe track is also calculated by following exactly the same procedure as for photons, with the only exception being that the track itself is excluded from the sum. Finally, the efficiency of the track-ISO<1 GeV cut for the probe track is compared in data and MC. The observed relative difference of 8%, independent of the track $p_{\rm T}$, is taken as an estimate of the systematic uncertainty due to data-MC differences in the track-ISO background efficiency.

Finally, the last source of systematic uncertainty in the background track-ISO efficiency is associated with the choice of an $E_{\rm T}$ threshold for selecting fake photons from a particular jet sample. The fake rate for jets is very small and, as a consequence, the MC dijet samples do not have enough statistics to yield a sufficient number of fake

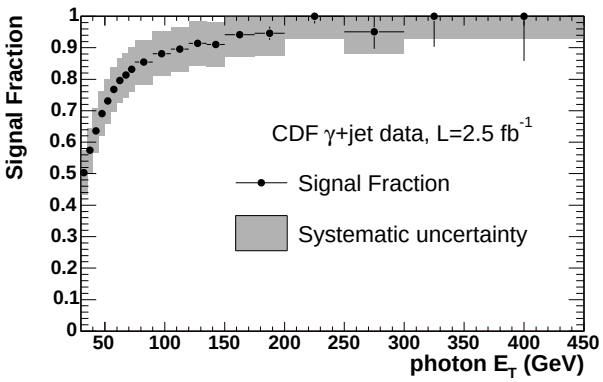

FIG. 7: The estimated signal fraction in the inclusive photon data. The shaded area is the total systematic uncertainty in the signal fraction.

photons after the selection cuts. To maximize the statistics, fake photons are accepted from each dijet sample if $E_{\rm T}>\hat{p}_{\rm T}$ where $\hat{p}_{\rm T}$ is the parton transverse momentum cutoff used in the event generation. Ideally, events with $E_{\rm T}>(\hat{p}_{\rm T}+\text{offset})$ should have been selected to avoid a bias due to the $\hat{p}_{\rm T}$ threshold effect. This is necessary because fake photons carry, on the average, only 90% of the energy of the original parton. Therefore, the procedure is biased toward selecting fakes originating from gluon jets produced by radiation, which are not limited by the $\hat{p}_{\rm T}$ threshold of hard scattering, and as a consequence toward lower background efficiencies. To obtain a conservative estimate of this effect, the threshold was lowered even more, thus accepting fake photons with $E_{\rm T}>F\times\hat{p}_{\rm T}$ where $F\sim$0.8-0.9, depending on $\hat{p}_{\rm T}$. By decreasing the threshold, the effect is overestimated, but this gives a conservative estimate of the associated uncertainty. The total systematic uncertainty of the background track-ISO efficiency is at the level of 10%-12% in the range of photon $E_{\rm T}$ from 15 GeV to 200 GeV, the range relevant to this analysis.

The background subtraction procedure has been tested with MC signal and fake events as well as with inclusive photon data. Tests with MC provide closure checks: the returned purity was 100% for signal events and 0% for fakes (within the corresponding uncertainties). The estimated photon purity for inclusive photon data as a function of the photon transverse energy is shown in Fig. 7 and is similar to the purity obtained in the inclusive photon cross section analysis [10]. The uncertainty in the signal fraction of the inclusive photon sample achieved with the track-ISO method is between ∼11% at low $E_{\rm T}$ and ∼5% at very high $E_{\rm T}$. Fig. 8 shows the estimated purity for the diphoton data as a function of the kinematic variables defined in Subsection V B.

TABLE III: Summary of the requirements applied to the generated MC events to define the denominator of the selection efficiency and the meaning of cross section measurement itself. y^γ is the photon rapidity [12].

Cuts	Selected $\gamma\gamma$ events
$E_{\rm T}^\gamma$	$\geq$ 15 GeV (1$^{\rm st}\gamma$), $\geq$ 17 GeV (2$^{\rm nd}\gamma$)
$\lvert y^\gamma\rvert$	$\leq$1.0 for both photons
Isolation	$\leq$2.0 GeV for both photons
$\Delta R(\gamma\gamma)$	$\geq$0.4
	No matching requirement between generated and reconstructed objects

B. Event Reconstruction and Selection Efficiency

The corrections for event reconstruction and selection efficiency were derived primarily from PYTHIA diphoton MC samples. The numerator of the efficiency is the number of events with two photons that pass all of the trigger criteria and selection cuts listed in Tables I and II. The definition of the cross section measurement is determined by the definition of the denominator of the efficiency. The denominator cuts are summarized in Table III. This work reports a cross section for isolated photons, so the selection of denominator events includes isolation. This isolation is found by summing over all generated hadrons and photons originating from the primary vertex within a cone of ΔR=0.4 around each photon.

For each kinematic quantity, one histogram of the reconstructed quantity and one of the quantity derived from generator variables are constructed. In the first iteration, the efficiency is computed as the ratio of these histograms. This ratio also corrects event migration in neighboring bins due to finite resolution. Events which pass the denominator cuts and have a reconstructed value for the histogrammed quantity but not a generator level value are assigned the reconstructed values as the best approximation to the generator level values. To improve accuracy, the efficiency calculation is iterated a second time. Once all corrections are applied to the data, including the efficiency, it is the best available representation of the true distribution. Then the PYTHIA events are reweighted so that the second iteration of the denominator histogram agrees with the corrected data. The purpose is to correct the PYTHIA distribution closer to the true distribution, making the efficiency more accurate. In practice, this does not have a large effect on any distribution (see Fig. 9). A third iteration changes the efficiency at the level of 1% or less and, therefore, only two iterations are applied.

The following corrections are applied to the efficiency:

- $Z^0 \to e^+e^-$ events in data and MC are compared to derive a correction to the photon ID efficiency reported by the MC. The correction is reported as a function of N_{vx} and of run periods. The correction is weighted by the period luminositites, and

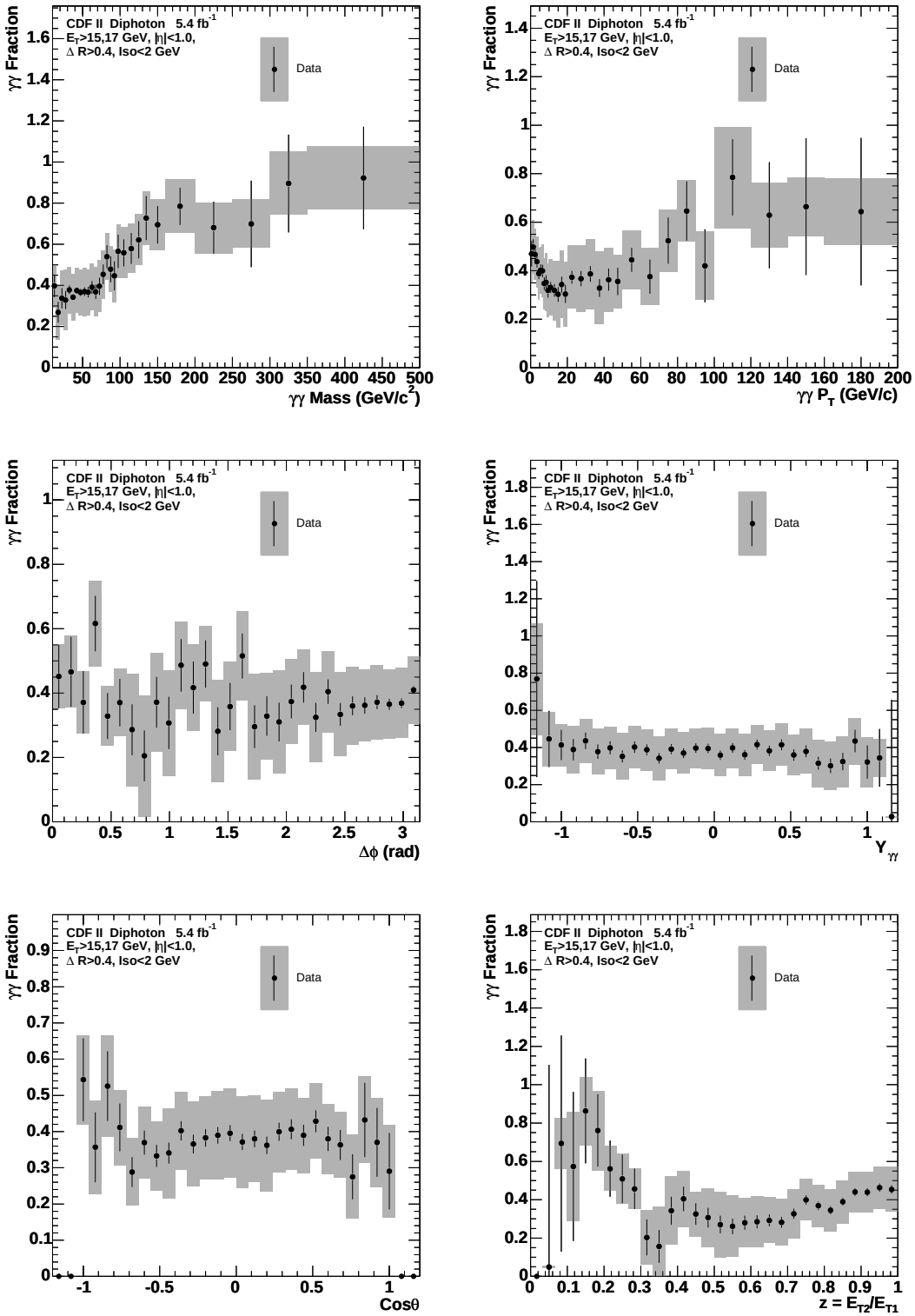

FIG. 8: The estimated signal fraction in the diphoton data as a function of several kinematic variables. The shaded area is the total systematic uncertainty in the signal fraction.

the observed N_{vx} distributions to find an overall multiplicative efficiency correction of 0.967 per photon. In addition, there is some indication of an $E_{\rm T}$-dependence, so the factor 0.967 is allowed to vary

linearly up to 1.0 between 40 and 80 GeV, and then is held constant at 1.0 above 80 GeV.

- A small correction is included near the E_{T} cut threshold due to the trigger turn-on curve. This is implemented as a factor of 0.98 at $E_{\mathrm{T}} = 15$ GeV, going linearly up to 1.0 at $E_{\mathrm{T}} = 18$ GeV. Ref. [10] concludes that there is no need for other corrections for the trigger.

- PYTHIA includes the underlying event, but NLO calculations do not. This makes the PYTHIA-based efficiency correction too large when comparing the isolated cross section to NLO predictions. It is too large since the UE causes events to be removed from the isolated denominator of the efficiency. A correction is derived by convoluting the PYTHIA UE isolation energy with the DIPHOX energy in the isolation cone [6]. This reduces the probability for the DIPHOX event to pass the isolation cuts. This effect is measured to be a factor of 0.88 per event which is then applied as a correction to the data.

The efficiency obtained for the kinematic quantities defined in Subsection V B is shown in Fig. 9. The typical efficiency is 40%.

In addition to the total systematic uncertainty arising from the background subtraction, whose details are discussed in Subsection IV A, the following systematic uncertainties are included in the cross section measurement.

- The Z^0-based efficiency correction has an uncertainty from several sources, including uncertainty in the amount of material leading to conversion events, which are rejected, and the difference between the electron and photon response to cuts. These are summarized as 1.8% below $E_{\mathrm{T}} = 40$ GeV, rising linearly to 3% at 80 GeV and fixed above that point. This increase completely covers the E_{T}–dependence in the photon ID efficiency mentioned above.

- The photon energy scale is varied and the change in the kinematic distribution is reported as an uncertainty. For the diphoton mass, the variation is 0 at $E_{\mathrm{T}} = 40$ GeV, rising linearly up to 1.5% at 80 GeV, then fixed above 80 GeV. These uncertainties are based on energy scale studies in the inclusive photon cross section measurement [29].

- A 3% uncertainty due to trigger efficiency is taken from Ref. [10].

- A 6% uncertainty (3% per photon) for underlying event correction is taken from Ref. [29].

- No uncertainty in the acceptance from variations in the ISR/FSR model is included since the primary mechanism for the effect is extra jets interfering with isolation. Both the numerator and denominator photons in the efficiency calculation are isolated, therefore the efficiency is immune to this effect, to leading order.

- No uncertainty in the efficiency due to the choice of the Q^2 scale is included because the primary mechanism of this effect is through the boosting of the final state. Since the efficiency's numerator and denominator are calculated with full kinematic requirements, the efficiency is immune to this effect to leading order.

The breakdown of the systematic uncertainties for the kinemaric quantities defined in Subsection V B is shown in Fig. 10. In all distributions, the dominant uncertainty comes from the background subtraction. The total systematic uncertainty is obtained by adding all individual components quadratically and averages near 30%.

C. Corrections and Tests with the $Z^0 \to e^+e^-$ Sample

The $Z^0 \to e^+e^-$ sample is used in this analysis for two purposes: 1) to set the energy scale in the CEM calorimeter and 2) to check the overall cross section normalization. The $Z^0 \to e^+e^-$ data sample is derived from the diphoton trigger dataset. The same global event selection as for the diphoton sample is applied. Two objects are required to pass a "photon-like electron" selection. The cuts applied are those of the standard photon selection, with modifications to allow for the electron track. The modifications are:

- The number of allowed tracks in the cluster is increased by 1.

- The leading track p_{T} cut is applied on the second-highest p_{T} track instead of the highest one.

- The track isolation is corrected by subtracting the leading track p_{T}.

- $0.8 < E/p < 1.2$ is required for the energy-to-momentum ratio of the leading track. (Events which fail this cut also tend to fail the CES χ^2 cut.)

The electrons are required to match EM objects passing the Level-1 and Level-2 trigger criteria (or trigger simulation for the MC). A high–luminosity sample of fully simulated and reconstructed PYTHIA $Z^0 \to e^+e^-$ events is used for MC.

The electromagnetic energy scale is set by tuning the reconstructed Z^0 mass to the world average [30] in both the data and the MC samples. The correction is applied as a function of time. It is applied before final event selection to account for a few events slightly below the energy threshold which the correction pushes above the threshold. The correction can only have a noticable effect on kinematic variables with rapidly falling spectra, related to the photon E_{T}, such as the diphoton mass. A 1.5%

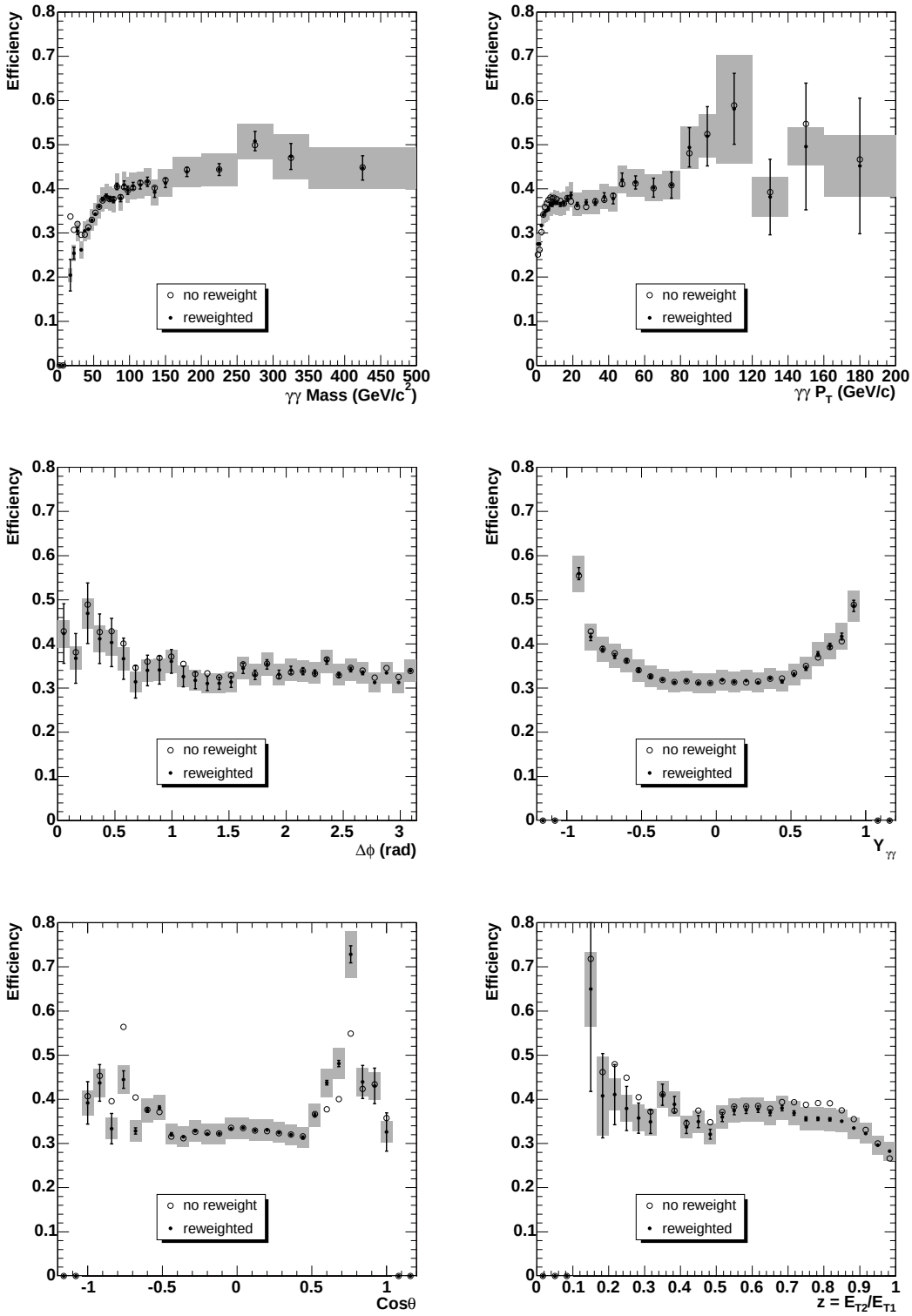

FIG. 9: The estimated efficiency as a function of several kinematic variables. The shaded area is the total systematic uncertainty in the efficiency.

systematic uncertainty due to energy scale is included, as mentioned in Subsection IV B.

The $Z^0 \to e^+e^-$ cross section is measured in order to check the cross section measurement procedures. This

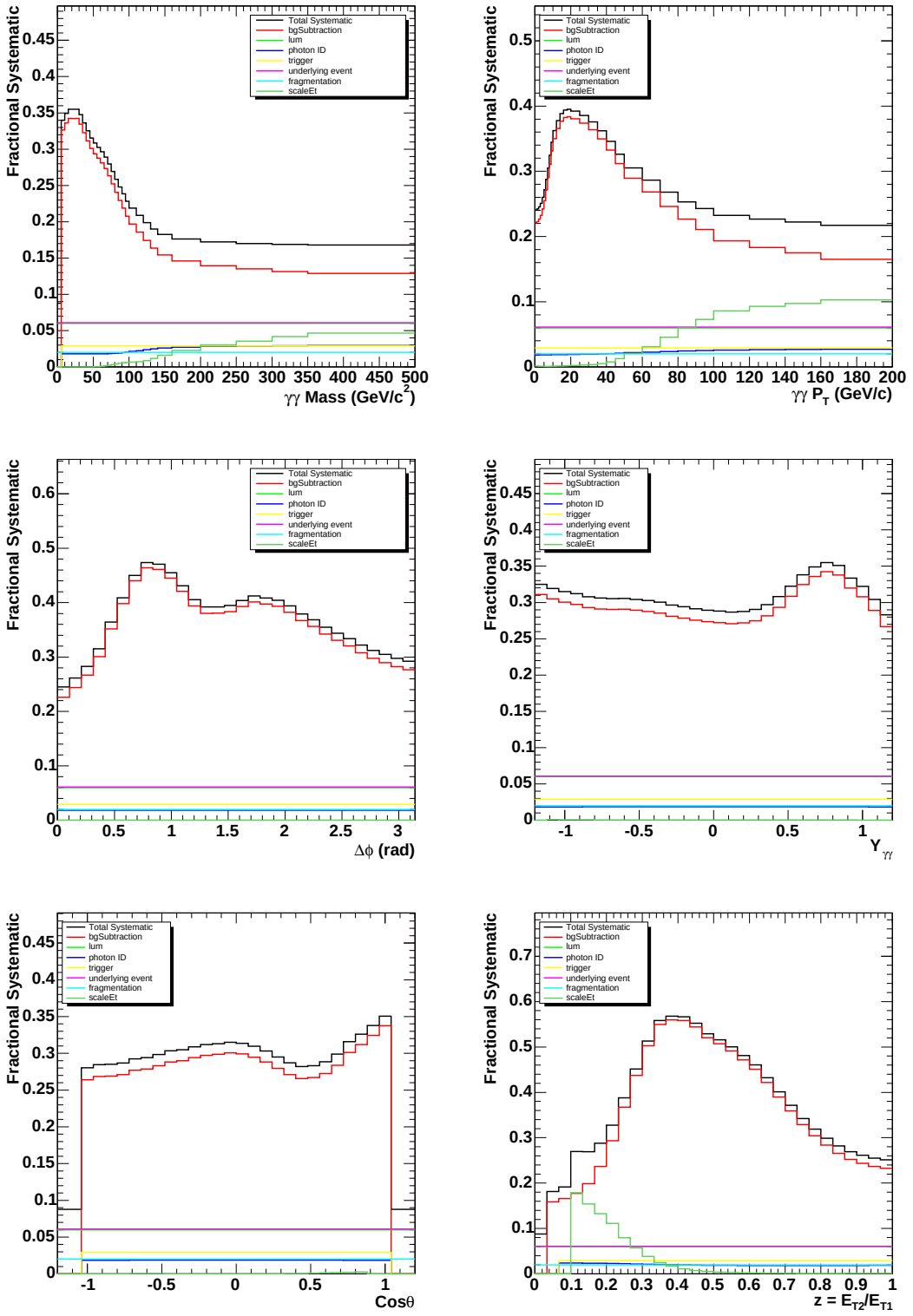

FIG. 10: The estimated systematic uncertainties in the cross section as a function of several kinematic variables.

measurement tests the trigger efficiency, the ability for the MC to predict the event selection efficiency, the efficiency corrections, and the luminosity. The cross section is measured for events with e^+e^- invariant mass between 65 and 115 GeV/c^2. The "photon-like electron" selection is applied and the efficiency from the PYTHIA MC is used.

The same photon efficiency corrections as in the diphoton cross section (see Subsection IV B) are applied. Since the photon–like electron cuts are used, it is assumed that the response is similar to photon response. The resulting $Z^0 \to e^+e^-$ cross section is found to be consistent with previous dedicated measurements and expectation from theory [31].

V. RESULTS

This Section presents the results of the cross section measurement. A brief description of the theoretical calculations is given first, then the comparisons for selected kinematic variables are shown and discussed. Tables with the measured cross section values are given in Appendix B.

A. Theoretical Calculations

The results of this measurement are compared with three theoretical predictions:

- A calculation using the PYTHIA program [3]. This is a parton–showering generator which features a realistic representation of the physics events in terms of observable particles. It includes initial and final state radiation and an underlying event model. PYTHIA implements a Leading-Order (LO) matrix element (ME) for direct diphoton production which includes the $q\bar{q} \to \gamma\gamma$ and $gg \to \gamma\gamma$ LO processes described, respectively, by diagrams (a) and (b) of Fig. 1. Significant contributions also arise from the processes $q\bar{q} \to \gamma\gamma g$ (diagrams (c) of Fig. 1) and $gq \to \gamma\gamma q$ (diagrams (d) of Fig. 1) where the second photon is emitted from an initial or final state quark according to the PYTHIA radiation model. These contributions were included in the calculation by running the program with a filter selecting diphoton events from inclusive γ+X events, where X is either a photon or a jet, with an efficiency of 0.025%. Fig. 11 shows the individual contributions to the cross section as a function of the diphoton invariant mass, transverse momentum and azimuthal difference. Initial-state radiation (ISR) photons, in particular, produce substantially different distributions than ME and final-state radiation (FSR) photons, having a harder transverse momentum spectrum and stronger low–$\Delta\phi$ tail in the azimuthal difference spectrum. In leading order, this can be attributed to the fact that FSR occurs in quark-gluon scattering [diagram (d) of Fig. 1], whereas ISR occurs both in $q\bar{q}$ annihilation [diagram (c) of Fig. 1] and quark-gluon scattering, and the luminosity of quark-gluon states falls off more rapidly with the parton momenta than the luminosity of $q\bar{q}$ states [6, 8]. The diphoton ME contributes 56% to the cross section, the processes $q\bar{q} \to g\gamma\gamma_{\rm ISR}$ and $gq \to q\gamma\gamma_{\rm ISR}$ 29%, and the process $gq \to q\gamma\gamma_{\rm FSR}$ 15%. Double radiation processes in minimum bias dijet events, such as $qq \to qq\gamma_{\rm ISR/FSR}\gamma_{\rm ISR/FSR}$, $q\bar{q} \to q\bar{q}\gamma_{\rm ISR/FSR}\gamma_{\rm ISR/FSR}$, $gq \to gq\gamma_{\rm ISR/FSR}\gamma_{\rm ISR/FSR}$, $q\bar{q} \to gg\gamma_{\rm ISR}\gamma_{\rm ISR}$ and $gg \to q\bar{q}\gamma_{\rm FSR}\gamma_{\rm FSR}$, were also examined but their overall contribution was estimated to only $\sim 3\%$ of the total, having no significant effect to any kinematical distribution. Therefore, these processes were not included in the PYTHIA calculation.

- A fixed Next-to-Leading-Order (NLO) calculation using the DIPHOX program [6]. This generator explictly includes parton fragmentation into photons [9], *i.e.* processes in which nearly all the energy of a parton is transformed into a photon. Direct production contributes 85% to the cross section and fragmentation 15%. The DIPHOX matrix element accounts for the $q\bar{q} \to \gamma\gamma$ and $gq \to \gamma\gamma q$ processes up to NLO, and LO for the $gg \to \gamma\gamma$ process, since this is already a second order process in the strong coupling. The NLO $gg \to \gamma\gamma$ contributions were examined with the GAMMA2MC program [7]. Fig. 12 shows an example of the uncorrected and corrected DIPHOX predictions in comparison with the measured cross section as a function of the diphoton invariant mass M. The corrected prediction is calculated by running DIPHOX without the LO $gg \to \gamma\gamma$ term and then adding the full LO+NLO $gg \to \gamma\gamma$ calculation from GAMMA2MC incoherently, since the initial state is different in gluon fusion than in the other processes. The correction of the total cross section for the NLO $gg \to \gamma\gamma$ contribution is nearly 10%, which is comparable with the experimental and theoretical uncertainties (see Table IV). Therefore, this correction was not applied to the DIPHOX calculation.

- A resummed NLO calculation using the RESBOS program [8]. Here the effects of soft gluon ISR in the NLO calculation are analytically resummed to all orders in the strong coupling and reach NNLL accuracy. The resultant prediction is smoothly matched to the fixed-order NLO result in the kinematic regions where the NLO matrix element is dominant. The RESBOS matrix element includes the $q\bar{q} \to \gamma\gamma$, $gq \to \gamma\gamma q$ and $gg \to \gamma\gamma$ processes up to NLO and it is adjusted so as to approximately account for fragmentation.

All calculations are done by Monte Carlo event generation and are subject to the experimental kinematic and isolation cuts. In the fixed-order NLO calculations the isolation cut is applied on parton variables and thus it only approximates the isolation cut appplied in the data and in PYTHIA. The RESBOS predictions are restricted in the diphoton invariant mass M range from $2m_b = 9$ GeV/c^2 to $2m_t = 350$ GeV/c^2 and they are shown up to

$M = 300$ GeV/c^2 in the plots of the mass distribution, where m_b and m_t are the masses of the bottom and top quarks, respectively.

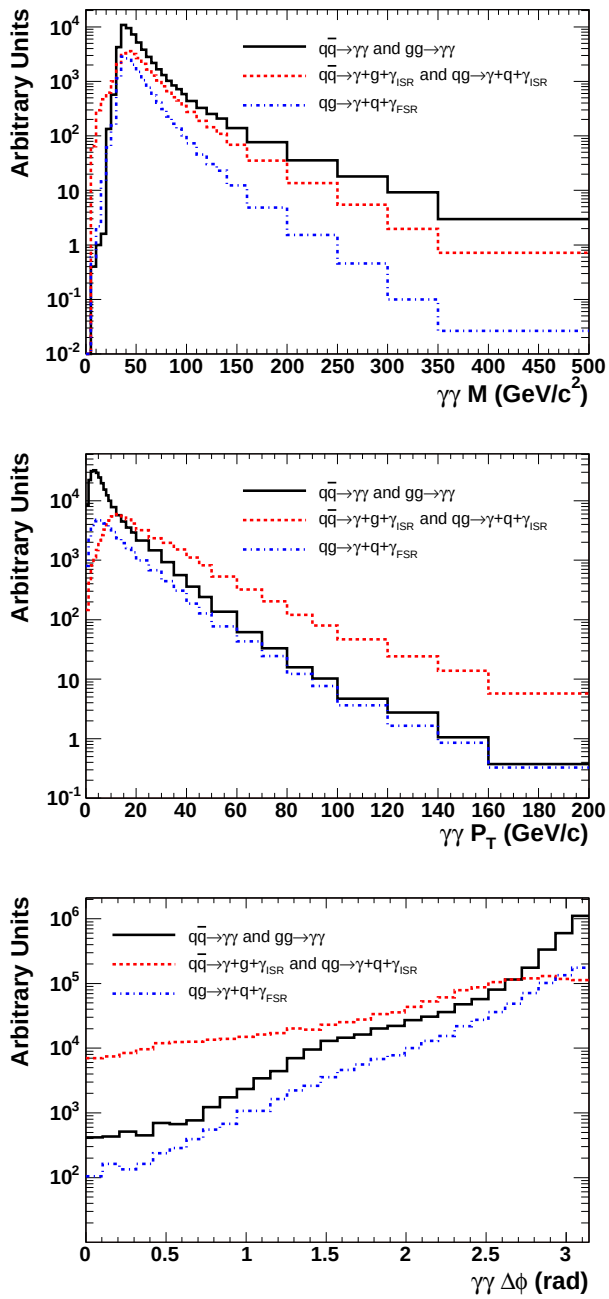

FIG. 11: The individual contributions to the cross section from events where both photons are generated according to the PYTHIA diphoton matrix element and from events where one photon originates from initial or final state radiation, as functions of the diphoton mass (top), transverse momentum (middle) and azimuthal difference (bottom).

NLO theoretical uncertainties are estimated for the choice of scale, representing the sensitivity to missing higher order terms, and for the PDFs. In DIPHOX the default renormalization, factorization and fragmentation scales are all set to $\mu = M/2$. In RESBOS the default renormalization and factorization scales are both set to $\mu = M$. In either case, all scales are varied by a factor of 2 up and down relative to the default choice and this is taken as a conservative estimate of the total scale uncertainty. The proton PDF set is the CTEQ6.1M set [32] for both DIPHOX and RESBOS. The corresponding uncertainty is estimated by varying the generated event weights within the 90% level uncertainties given by the 20 CTEQ6.1M eigenvectors.

The measured total cross section is shown in Table IV together with the predictions from the three theoretical calculations. All calculations are consistent with the size of the measured cross section within the experimental uncertainties.

B. Kinematic Variables

The complete description of the reaction $h_1+h_2 \to \gamma_1+\gamma_2+X$, where $h_{1,2}$ are hadrons, requires five independent kinematic variables. A suitable choice consists of the invariant mass

$$M = \sqrt{2p_{\mathrm{T}\gamma 1}p_{\mathrm{T}\gamma 2}[\cosh(y_{\gamma 1}-y_{\gamma 2})-\cos(\phi_{\gamma 1}-\phi_{\gamma 2})]} \tag{2}$$

the transverse momentum

$$P_{\mathrm{T}} = \sqrt{p_{\mathrm{T}\gamma 1}^2 + p_{\mathrm{T}\gamma 2}^2 + 2p_{\mathrm{T}\gamma 1}p_{\mathrm{T}\gamma 2}\cos(\phi_{\gamma 1}-\phi_{\gamma 2})} \tag{3}$$

the rapidity

$$Y_{\gamma\gamma} = \tanh^{-1}\frac{p_{\mathrm{T}\gamma 1}\sinh y_{\gamma 1} + p_{\mathrm{T}\gamma 2}\sinh y_{\gamma 2}}{p_{\mathrm{T}\gamma 1}\cosh y_{\gamma 1} + p_{\mathrm{T}\gamma 2}\cosh y_{\gamma 2}} \tag{4}$$

the azimuthal difference

$$\Delta\phi = |\phi_{\gamma 1}-\phi_{\gamma 2}| \mod \pi \tag{5}$$

of the photon pair in the laboratory frame [12], and the cosine of the polar angle θ of the 1st photon in the Collins-Soper frame [33]. This is defined as the rest frame of the photon pair chosen so that (a) the 3-momenta $\vec{p}_{h_1}$ and $\vec{p}_{h_2}$ of the initial hadrons lie in the Oxz plane (with positive x) and (b) the z axis bisects the angle between $\vec{p}_{h_1}$ and $-\vec{p}_{h_2}$. This variable is generally determined by [33]

$$\cos\theta = \frac{2p_{\mathrm{T}\gamma 1}p_{\mathrm{T}\gamma 2}\sinh(y_{\gamma 1}-y_{\gamma 2})}{M\sqrt{M^2+P_{\mathrm{T}}^2}} \tag{6}$$

For photons emitted at large angles with respect to the beam, $\cos\theta \approx \tanh[(y_{\gamma 1}-y_{\gamma 2})/2]$ in the limit $P_{\mathrm{T}} \to 0$. In the above equations $p_{\mathrm{T}\gamma \mathrm{i}}$, $y_{\gamma i}$ and $\phi_{\gamma i}$ are the transverse

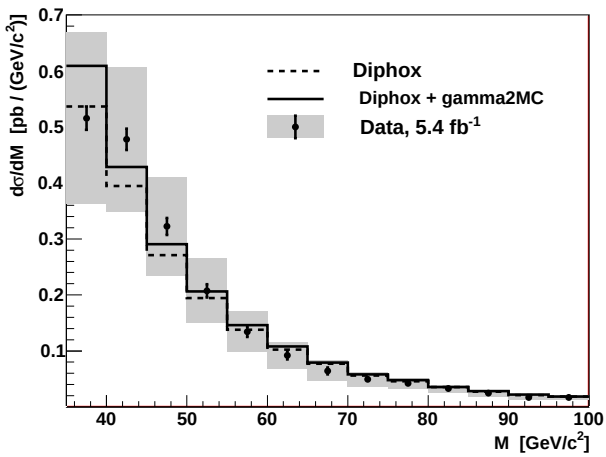

FIG. 12: The measured cross section as a function of the diphoton mass in comparison with the DIPHOX predictions without and with the NLO $gg \to \gamma\gamma$ correction, calculated by the GAMMA2MC program. The shaded area is the total systematic uncertainty in the data.

momentum, rapidity and azimuth of photon i, respectively, with i=1, 2.

The set of $\{M, P_{\rm T}, Y_{\gamma\gamma}\}$ describes the kinematics of the diphoton system and, therefore, of possible heavy particles decaying into a photon pair, such as a Higgs boson. The existence of such a particle would manifest as a peak in the distribution of the invariant mass M. The results of this analysis are presented in the form of cross sections differential in each of the five kinematic variables $\{M, P_{\rm T}, \Delta\phi, Y_{\gamma\gamma}, \cos\theta\}$ and in the variable $z = p_{{\rm T}\gamma 2}/p_{{\rm T}\gamma 1}$, the ratio of sub-leading to leading photon transverse momentum ($0 \le z \le 1$). Three kinematic cases are examined:

- Differential cross sections without additional kinematic cuts. No kinematic cut other than those listed in Table III is applied. The results of this case are presented in Subsection V C.
- Differential cross sections for $P_{\rm T} < M$. The kinematics in this case are similar to the diphoton decay of a heavy particle, such as a Higgs boson, produced in events of moderate parton activity. At the Tevatron, prompt photon pairs are almost entirely produced in this case by low-$P_{\rm T}$ quark-antiquark annihilation. The results of this case are presented in Subsection V D.
- Differential cross sections for $P_{\rm T} > M$. The importance of high-$P_{\rm T}$ contributions from gluon-gluon fusion, fragmentations and ISR is enhanced in this case. The results of this case are presented in Subsection V E.

The oveflow data entries are excluded from the M and $P_{\rm T}$ histograms, to keep the cross section definition consistent for the data and the theories at the highest bins.

TABLE IV: The total diphoton production cross section obtained from the measurement and from the theoretical calculations. The PYTHIA $\gamma\gamma$ calculation involves only the $q\bar{q} \to \gamma\gamma$ and $gg \to \gamma\gamma$ processes. The PYTHIA $\gamma\gamma + \gamma$j calculation includes also the $q\bar{q} \to \gamma\gamma g$ and $gq \to \gamma\gamma q$ processes.

	Cross section (pb)
Data	$12.47 \pm 0.21_{\rm stat} \pm 3.74_{\rm syst}$
RESBOS	$11.31 \pm 2.45_{\rm syst}$
DIPHOX	$10.58 \pm 0.55_{\rm syst}$
PYTHIA $\gamma\gamma + \gamma$j	9.19
PYTHIA $\gamma\gamma$	5.03

For each kinematic variable, the following plots are presented:

- The measured and calculated cross sections as functions of the selected variable. Each of these plots includes the predictions of all three calculations, for comparison, and shows only the uncertainties of the data. The prediction of the PYTHIA $\gamma\gamma$ calculation, involving only the $q\bar{q} \to \gamma\gamma$ and $gg \to \gamma\gamma$ processes, is also shown in these plots, to be compared with the PYTHIA $\gamma\gamma + \gamma$j calculation (j=jet), which includes also the $q\bar{q} \to \gamma\gamma g$ and $gq \to \gamma\gamma q$ processes.
- The relative deviations of the data from each calculation, in the form (data−theory)/theory, as functions of the selected variable. These plots show the comparison of the data with each calculation separately and include the uncertainties of the NLO predictions. No relative deviations are shown for the PYTHIA $\gamma\gamma$ calculation. The benchmark parton showering MC calculation, compared in detail with the data, is PYTHIA $\gamma\gamma + \gamma$j.

C. Differential Cross Sections Without Additional Kinematic Cut

Fig. 13 shows the results for $d\sigma/dM$ and $d\sigma/dP_{\rm T}$. The mass spectrum peaks at $M = 2\sqrt{E_{\rm T1}^{min} E_{\rm T2}^{min}} \approx 32$ GeV/c^2. All three theoretical predictions for $d\sigma/dM$ are in reasonable agreement with the data, within uncertainties, except in the region 6 GeV/$c^2 < M < 32$ GeV/c^2 below the mass peak. The low mass limit of 6 GeV/c^2 is set by the $\Delta R(\gamma\gamma)$ and $E_{\rm T}^{\gamma}$ cuts. This region is rich in events coming from gluon scattering and fragmentation. All three predictions underestimate the data in this region.

The excess of the data over all three predictions for M below the peak of the mass spectrum is reflected in the region 20 GeV/$c < P_{\rm T} <$ 50 GeV/c of the $P_{\rm T}$ spectrum, which has a shoulder around $P_{\rm T} = p_{\rm T2}^{min} + p_{\rm T1}^{min} = 32$ GeV/c (the so-called "Guillet shoulder"). This arises from a collinear enhancement for the two photons in the fragmentation processes which, however, is suppressed by the $\Delta R(\gamma\gamma)$ cut. The RESBOS predictions for $d\sigma/dP_{\rm T}$ are in overall

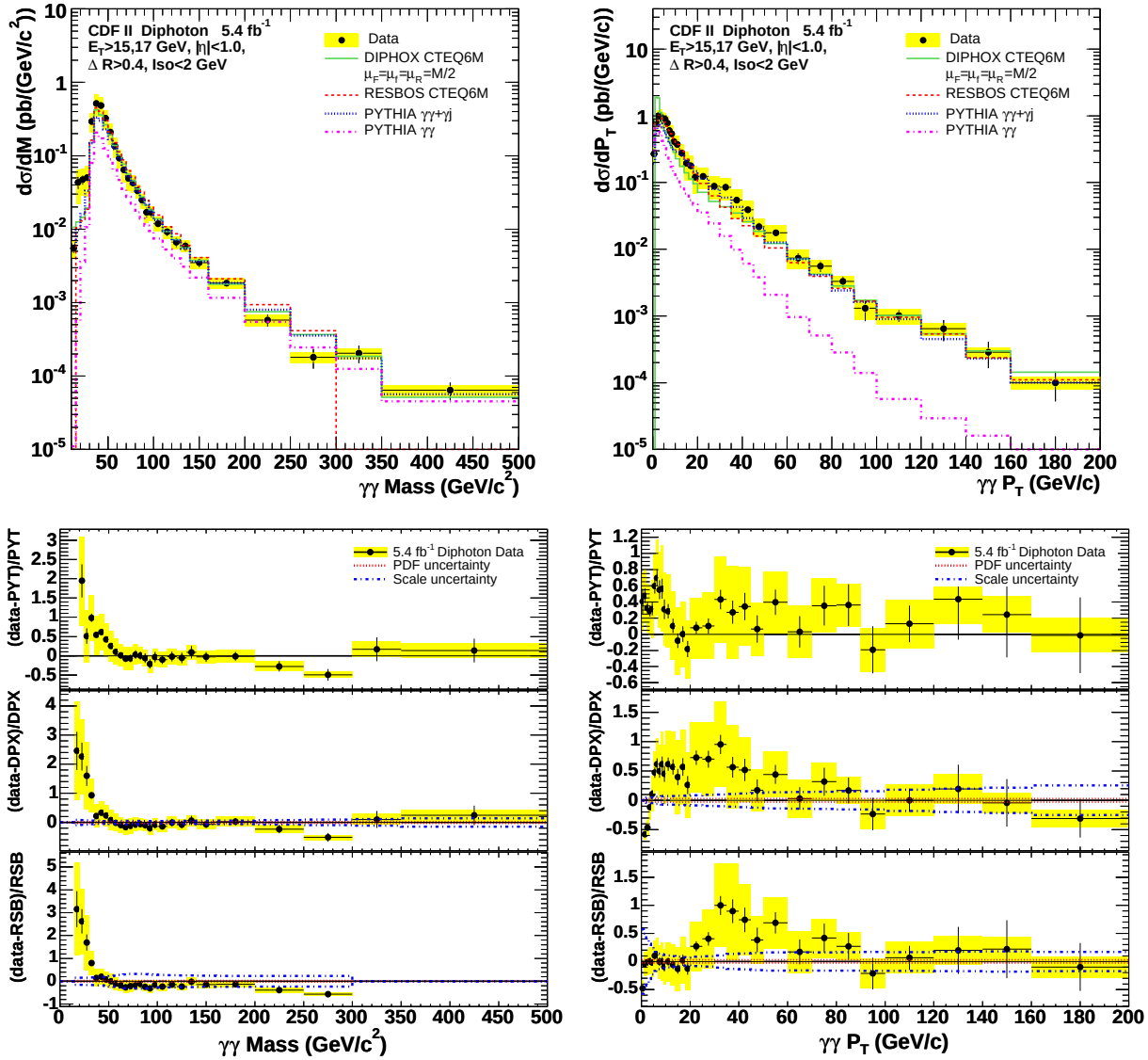

FIG. 13: The cross section as a function of the diphoton invariant mass (left) and transverse momentum (right). **Top:** the absolute cross section values. **Bottom:** the relative deviations of the data from the predictions. *Note:* the vertical axes scales differ between relative deviation plots. The shaded area is the total systematic uncertainty in the data.

agreement with the data, within uncertainties, except in this region. The DIPHOX prediction underestimates the data, in addition, for $P_{\rm T}$<20 GeV/c, where the resummation effects implemented in RESBOS provide a better description. The PYTHIA prediction underestimates the data at very low $P_{\rm T}$, $P_{\rm T}$<10 GeV/c, showing that the LL resummation of parton showering is less accurate than the NNLL resummation implemented in RESBOS. The PYTHIA prediction is in reasonably good agreement with the data, within uncertainties, in the rest of the $P_{\rm T}$ range due to the $q\bar{q} \to g\gamma\gamma_{\rm ISR}$ and $gq \to q\gamma\gamma_{\rm ISR}$ processes which make the PYTHIA $P_{\rm T}$ spectrum sufficiently hard (see the middle plot of Fig. 11).

Fig. 14 shows the results for $d\sigma/d\Delta\phi$ and $d\sigma/dY_{\gamma\gamma}$. The $\Delta\phi$ spectrum peaks at $\Delta\phi$=π, corresponding to vanishing diphoton $P_{\rm T}$, and the $Y_{\gamma\gamma}$ spectrum at $Y_{\gamma\gamma}$=0, corresponding to vanishing diphoton momentum $P_{\rm z}$ parallel to the proton beam. While all three predictions agree fairly well with the measured $d\sigma/dY_{\gamma\gamma}$, within uncertainties, all three of them underestimate the data in the low end of the $\Delta\phi$ spectrum. This region is dominated by events with low mass and high $P_{\rm T}$. The RESBOS prediction provides the best description of the measured $d\sigma/d\Delta\phi$ for $\Delta\phi$>2.5 rad, where soft gluon resummation is important. PYTHIA provides the best description in the region 1 rad<$\Delta\phi$<2.5 rad where the $q\bar{q} \to g\gamma\gamma_{\rm ISR}$ and $gq \to q\gamma\gamma_{\rm ISR}$ processes are the most important (see the bottom plot of Fig. 11).

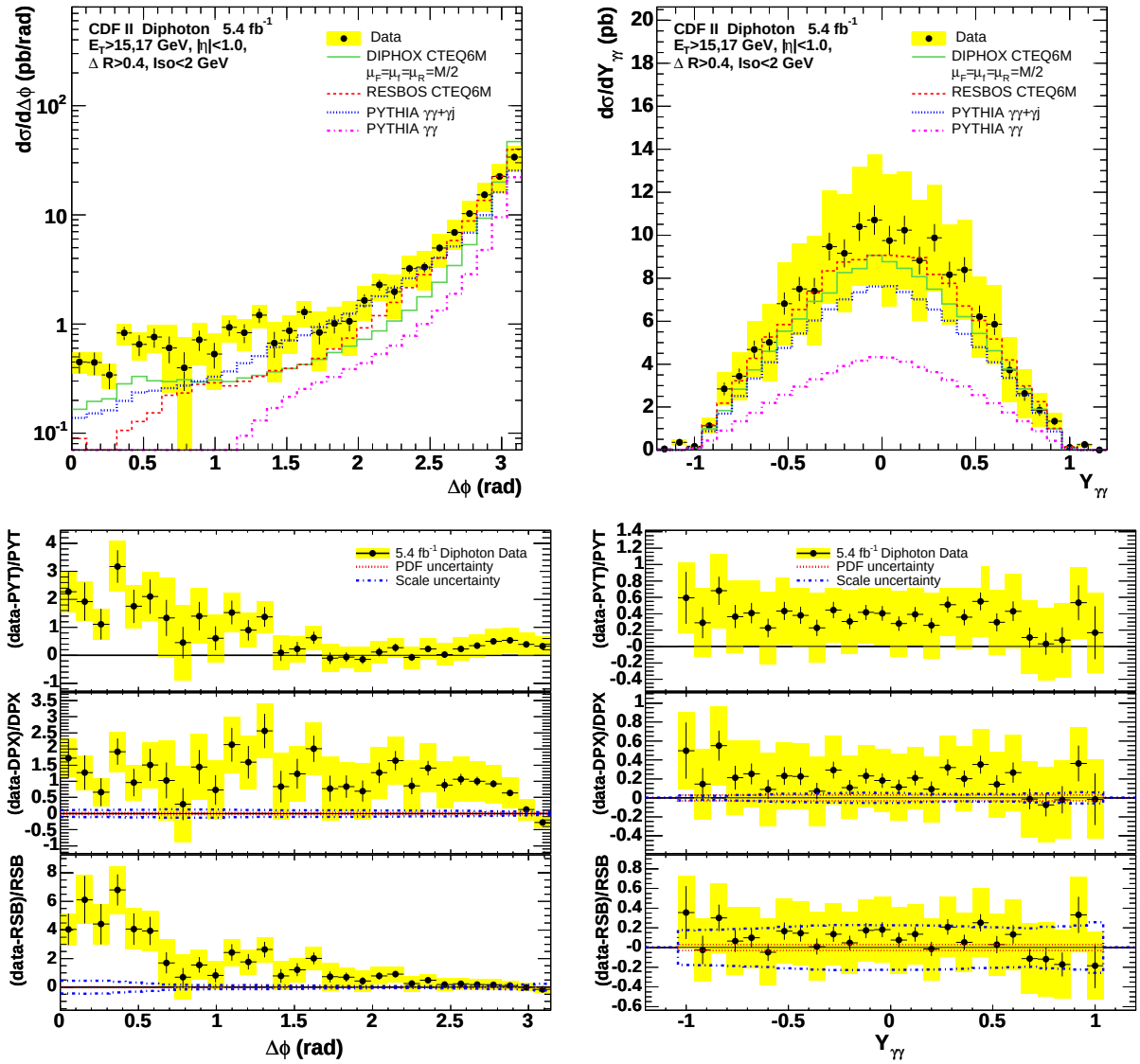

FIG. 14: The cross section as a function of the diphoton azimuthal distance (left) and of the diphoton rapidity (right). **Top:** the absolute cross section values. **Bottom:** the relative deviations of the data from the predictions. *Note:* the vertical axes scales differ between relative deviation plots. The shaded area is the total systematic uncertainty in the data.

Fig. 15 shows the results for $d\sigma/d\cos\theta$ and $d\sigma/dz$. All three predictions agree with the data, within uncertainties. Exceptions are the predictions of all three calculations underestimating the data in the two ends of the $\cos\theta$ spectrum, where again gluon scattering processes and associated fragmentation are expected to dominate [8].

In general, all three calculations reproduce most of the main features of the data, as observed in the earlier diphoton cross section measurements [10, 11]. However, depending on their approximations, they display differences with each other and with the data in certain kinematic regions. There is a problem common to all three calculations in the description of events with very low diphoton mass, low azimuthal distance and diphoton transverse momentum in the region of the "Guillet shoulder". Such events include fragmentation at a relatively high rate. The PYTHIA $\gamma\gamma$ calculation fails completely to describe the data both in the scale, where it is low by a factor of 2.5, and in the shape, particularly of the P_{T}, $\Delta\phi$ and z distributions, where it predicts a much softer spectrum than the data. This is in agreement with the conclusion of Ref. [10] which tested only PYTHIA $\gamma\gamma$ as a parton showering MC prediction.

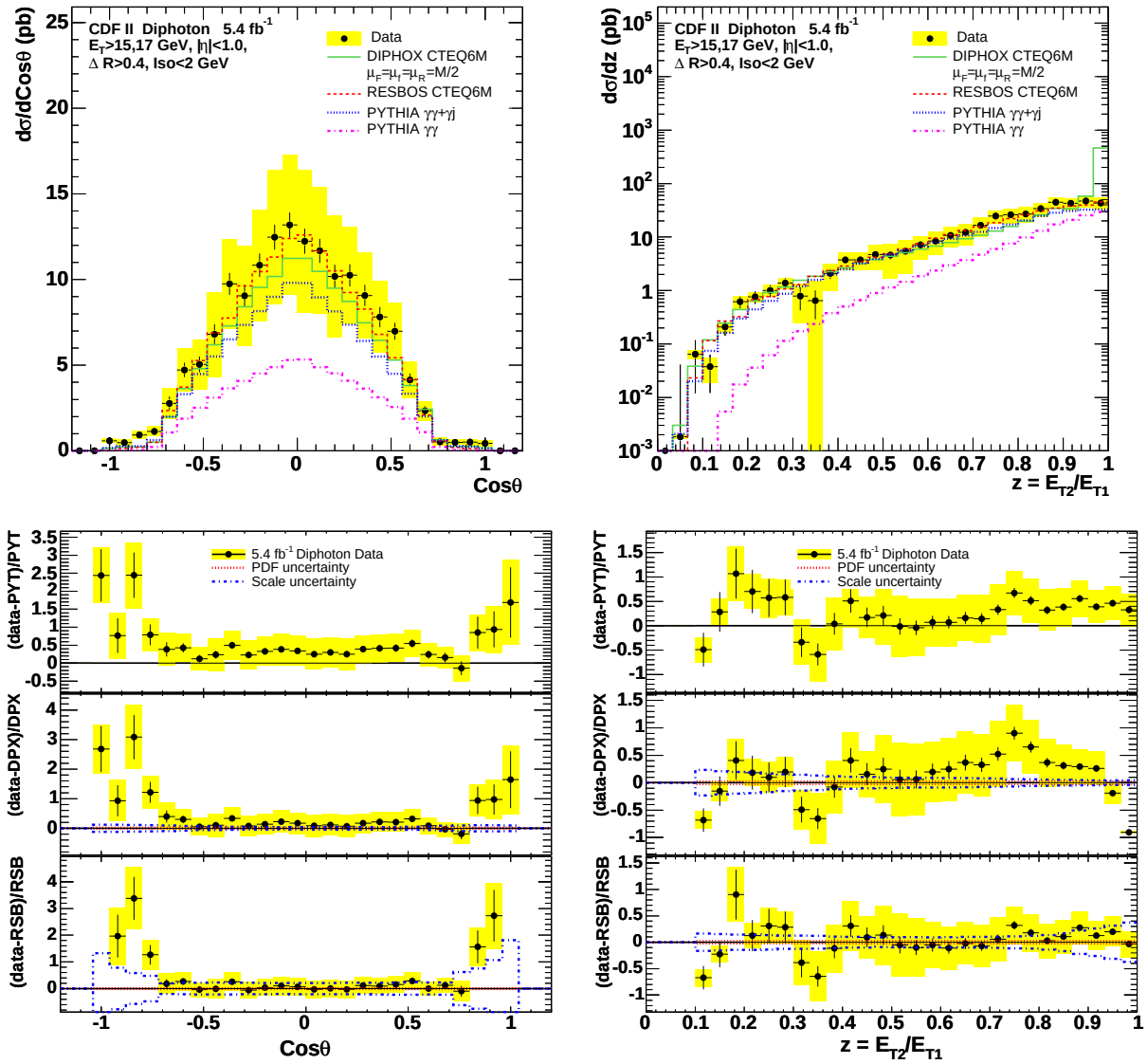

FIG. 15: The cross section as a function of the cosine of the polar angle in the Collins-Soper frame (left) and of the ratio of the subleading photon $E_{\rm T}$ to leading photon $E_{\rm T}$ (right). **Top:** the absolute cross section values. **Bottom:** the relative deviations of the data from the predictions. *Note:* the vertical axes scales differ between relative deviation plots. The shaded area is the total systematic uncertainty in the data.

D. Differential Cross Sections for $P_{\rm T}<M$ Kinematics

Fig. 16 shows the results for $d\sigma/dM$ and $d\sigma/dP_{\rm T}$ for $P_{\rm T}<M$. The low tail of the mass spectrum, in the region 6 GeV/c^2<M<32 GeV/c^2, and the shoulder of the $P_{\rm T}$ spectrum, in the region 20 GeV/c<$P_{\rm T}$<50 GeV/c, are now eliminated. The agreement between the data and all three predictions is improved in this case. However, DIPHOX still underestimates the data for $P_{\rm T}$<40 GeV/c and similarly PYTHIA still underestimates the data for $P_{\rm T}$<10 GeV/c, thus showing the importance of NNLL low–$P_{\rm T}$ resummation in this case as well.

Fig. 17 shows the results for $d\sigma/d\Delta\phi$ and $d\sigma/dY_{\gamma\gamma}$ for $P_{\rm T}<M$. The tail of the $\Delta\phi$ spectrum for $\Delta\phi<\pi/2$ is now weaker but the measured cross section is underestimated by all three predictions, as in the case of unconstrained kinematics.

Fig. 18 shows the results for $d\sigma/d\cos\theta$ and $d\sigma/dz$ for $P_{\rm T}<M$. The results are similar to the case of unconstrained kinematics. Generally, all three calculations agree with the data, within uncertainties. Exceptions are again the predictions of all three calculations in the two ends of the $\cos\theta$ spectrum, where they underestimate the data.

In general, events with kinematics similar to the de-

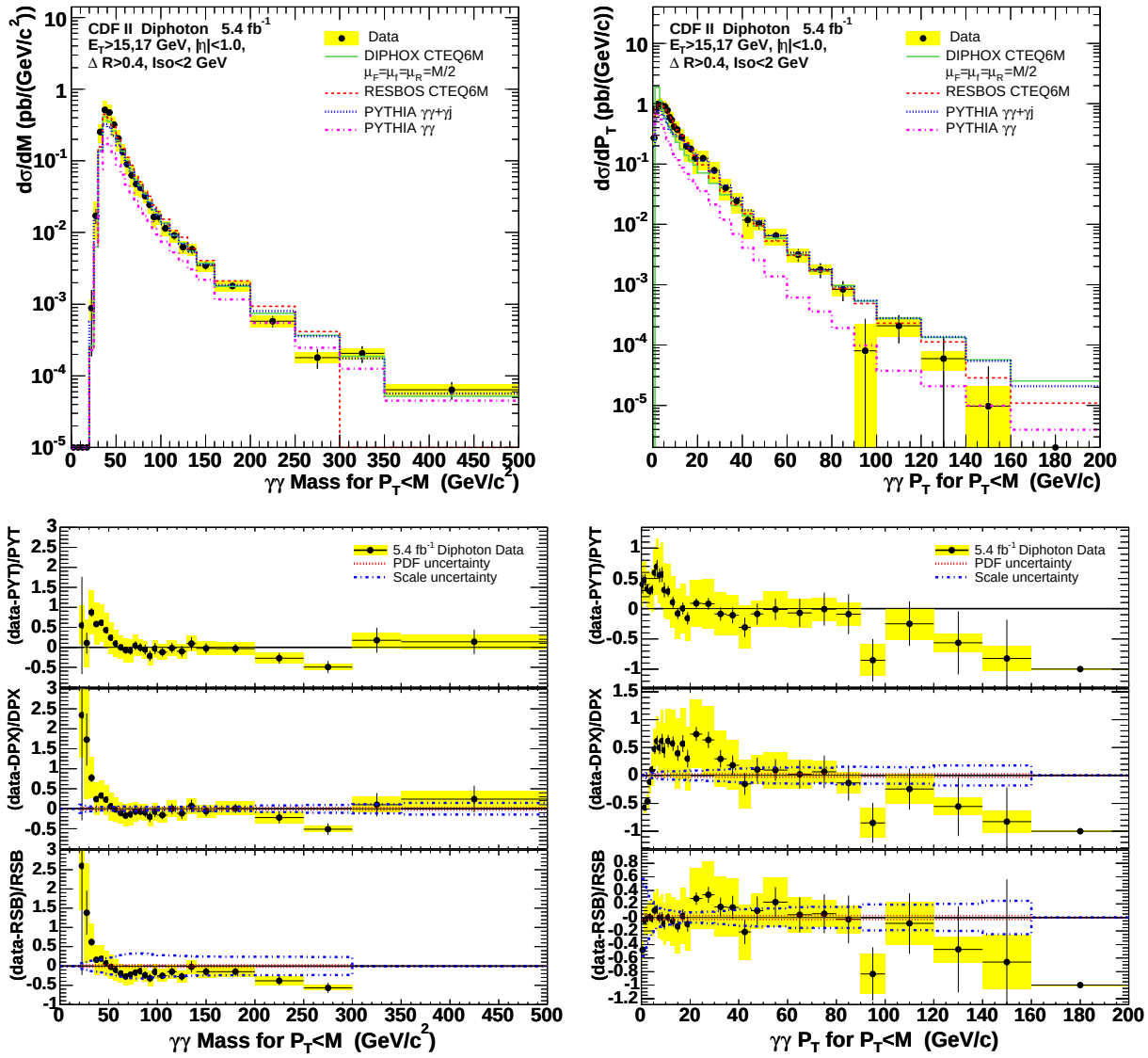

FIG. 16: The cross section as a function of the diphoton invariant mass (left) and transverse momentum (right) for $P_{\rm T}<M$. **Top:** the absolute cross section values. **Bottom:** the relative deviations of the data from the predictions. *Note:* the vertical axes scales differ between relative deviation plots. The shaded area is the total systematic uncertainty in the data.

cay of a heavy particle with low transverse momentum into a photon pair, such as gg→H→$\gamma\gamma$ production and decay, are better described by the theory than events with low mass and high transverse momentum. This is also observed in Ref. [11] which examines only the case of $P_{\rm T}<M$. This observation is important for current searches of yet undiscovered particles with a diphoton decay signature. The PYTHIA $\gamma\gamma$ calculation again fails to describe the data both in the scale and in the shape, in agreement with the conclusion of Ref. [11] which tested only PYTHIA $\gamma\gamma$ as a parton showering MC prediction.

E. Differential Cross Sections for $P_{\rm T}>M$ Kinematics

Fig. 19 shows the results for $d\sigma/dM$ and $d\sigma/dP_{\rm T}$ for $P_{\rm T}>M$. Both spectra are depleted in this case: the mass spectrum for $M>200$ GeV/c^2 and the transverse momentum spectrum for $P_{\rm T}<20$ GeV/c. All three calculations underestimate the data.

Fig. 20 shows the results for $d\sigma/d\Delta\phi$ and $d\sigma/dY_{\gamma\gamma}$ for $P_{\rm T}>M$. The $\Delta\phi$ spectrum is strongly suppressed for $\Delta\phi>\pi/2$. Again, the measured cross section is underestimated by all three calculations.

Fig. 21 shows the results for $d\sigma/d\cos\theta$ and $d\sigma/dz$ for $P_{\rm T}>M$. In contrast with the unconstrained kinematics

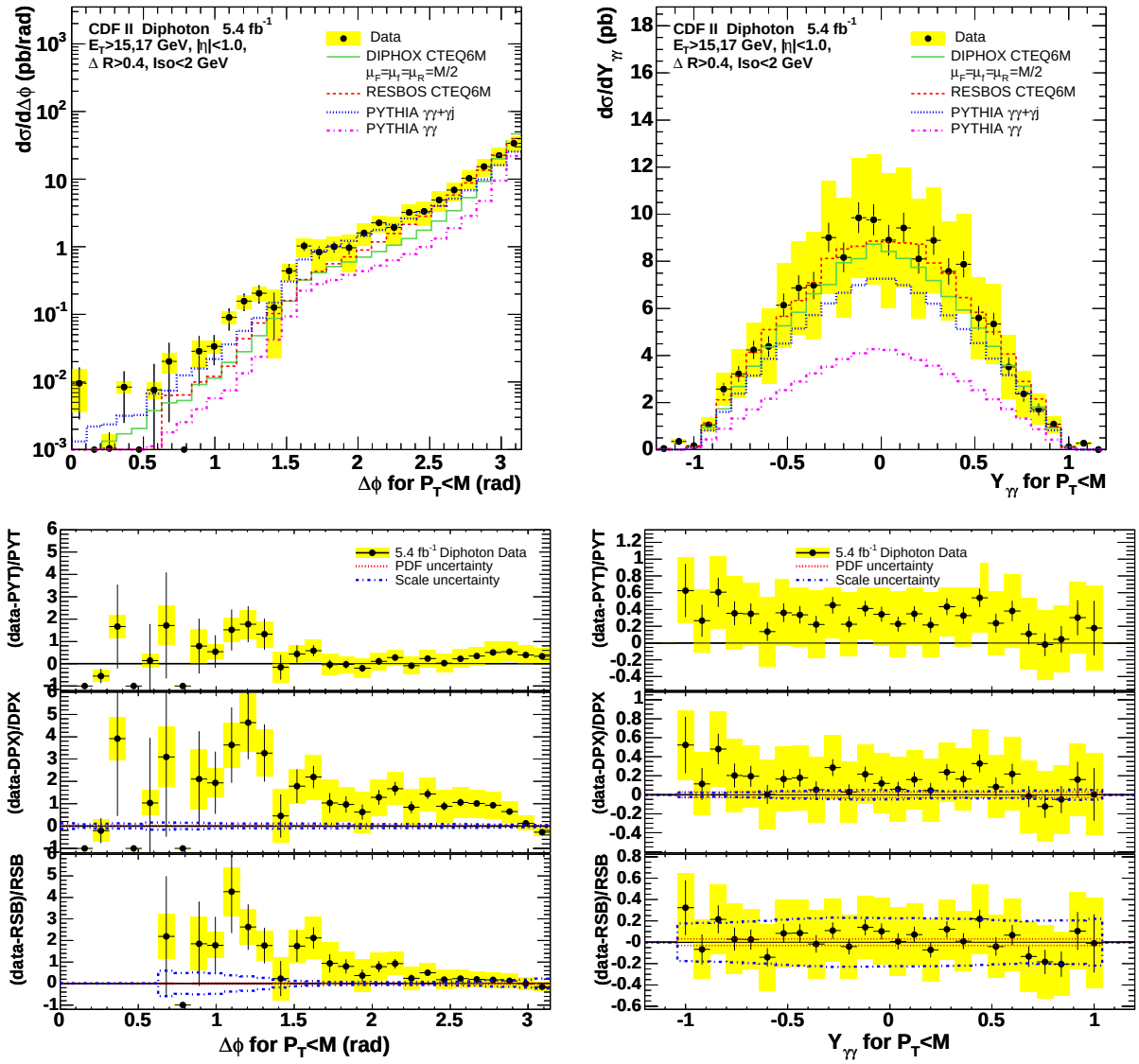

FIG. 17: The cross section as a function of the diphoton azimuthal distance (left) and of the diphoton rapidity (right) for $P_{\rm T}<M$. **Top:** the absolute cross section values. **Bottom:** the relative deviations of the data from the predictions. *Note:* the vertical axes scales differ between relative deviation plots. The shaded area is the total systematic uncertainty in the data.

and the $P_{\rm T}<M$ kinematics, in this case all three calculations underestimate the data through the full ranges of the $\cos\theta$ and z spectra.

In general, events with low diphoton mass and high diphoton transverse momentum, mainly coming from fragmentation, are not well described by the examined calculations. This observation is important for measurements under conditions where contributions from such events are strong, as in the LHC [1].

VI. CONCLUSIONS

In summary, the prompt diphoton production cross section, differential in kinematic variables sensitive to the dynamics of the reaction mechanism, is measured using data corresponding to an integrated of luminosity 5.36 fb^{-1} collected with the CDF II detector. The large size of the data sample allows for scanning a much more extended phase space and with a better statistical precision than in earlier measurements. Using a novel technique for the background subtraction, based on the track isolation, the overall systematic uncertainty is limited to about 30% on average.

The results of the measurement are compared with

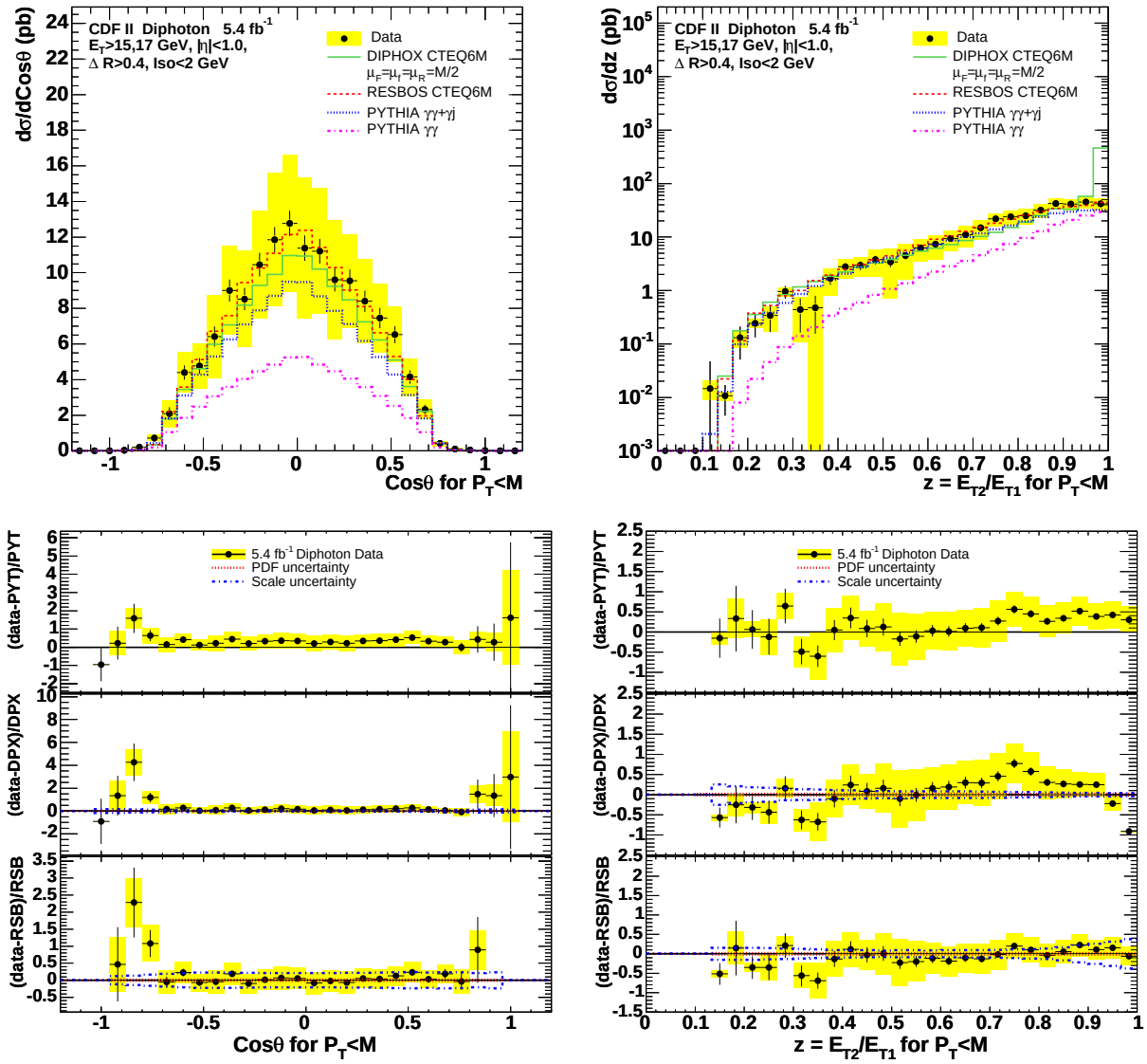

FIG. 18: The cross section as a function of the cosine of the polar angle in the Collins-Soper frame (left) and of the ratio of the subleading photon $E_{\rm T}$ to leading photon $E_{\rm T}$ (right) for $P_{\rm T}<M$. **Top:** the absolute cross section values. **Bottom:** the relative deviations of the data from the predictions. *Note:* the vertical axes scales differ between relative deviation plots. The shaded area is the total systematic uncertainty in the data.

three state-of-the-art calculations, applying complementary techniques in modeling the reaction. All three calculations describe events with large diphoton mass and small diphoton transverse momentum fairly well, where the kinematics is similar to the decay of a low-$P_{\rm T}$ heavy particle, such as the Higgs boson, decaying into a photon pair. Exceptions are kinematic regions where gluon interactions and the associated fragmentations of quarks into photons are expected to be important, such as the low mass and azimuthal difference regions and the region of the "Guillet shoulder" at moderate transverse momentum. All three calculations underestimate the data in those regions. Although the DIPHOX calculation explicitly includes a fragmentation model, it fails to reproduce the data in those sensitive regions, possibly because of the approximate nature of the requirement of photon isolation in the DIPHOX framework. This requirement is mostly responsible for the suppression of fragmentation contributions and is applied using hadron variables in the data but using parton variables in DIPHOX. The low transverse momentum and large azimuthal difference regions, where resummation in the diphoton transverse momentum is important, are best described by RESBOS, as expected from the analytical resummation implemented in this calculation. Photon radiation, especially from the initial state quarks, in addition to the prompt photon

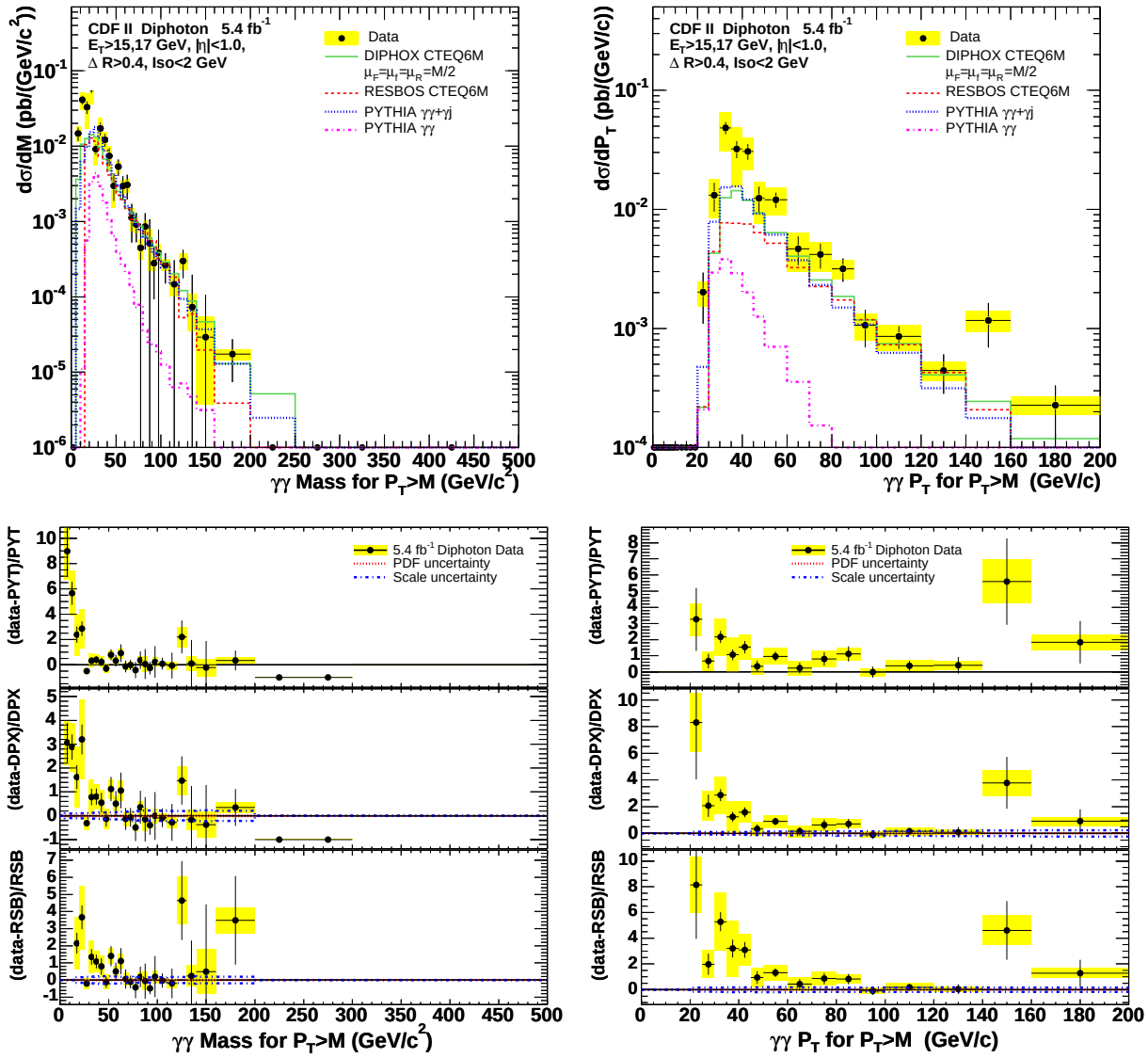

FIG. 19: The cross section as a function of the diphoton invariant mass (left) and transverse momentum (right) for $P_{\rm T}>M$. **Top:** the absolute cross section values. **Bottom:** the relative deviations of the data from the predictions. *Note:* the vertical axes scales differ between relative deviation plots. The shaded area is the total systematic uncertainty in the data.

production at the hard scattering, is for the first time shown to play a very important role in the parton showering PYTHIA calculation in order to bring the prediction into reasonable agreement with the data.

VII. ACKNOWLEDGEMENTS

We thank the Fermilab staff and the technical staffs of the participating institutions for their vital contributions. We also thank P. Nadolsky, C.-P. Yuan, Z. Li, J.-P. Guillet, C. Schmidt and S. Mrenna for their valuable help in the theoretical calculations. This work was supported by the U.S. Department of Energy and National Science Foundation; the Italian Istituto Nazionale di Fisica Nucleare; the Ministry of Education, Culture, Sports, Science and Technology of Japan; the Natural Sciences and Engineering Research Council of Canada; the National Science Council of the Republic of China; the Swiss National Science Foundation; the A.P. Sloan Foundation; the Bundesministerium für Bildung und Forschung, Germany; the Korean World Class University Program, the National Research Foundation of Korea; the Science and Technology Facilities Council and the Royal Society, UK; the Institut National de Physique Nucleaire et Physique des Particules/CNRS; the Russian Foundation for Basic Research; the Ministerio de Ciencia e Innovación, and Programa Consolider-Ingenio 2010, Spain; the Slo-

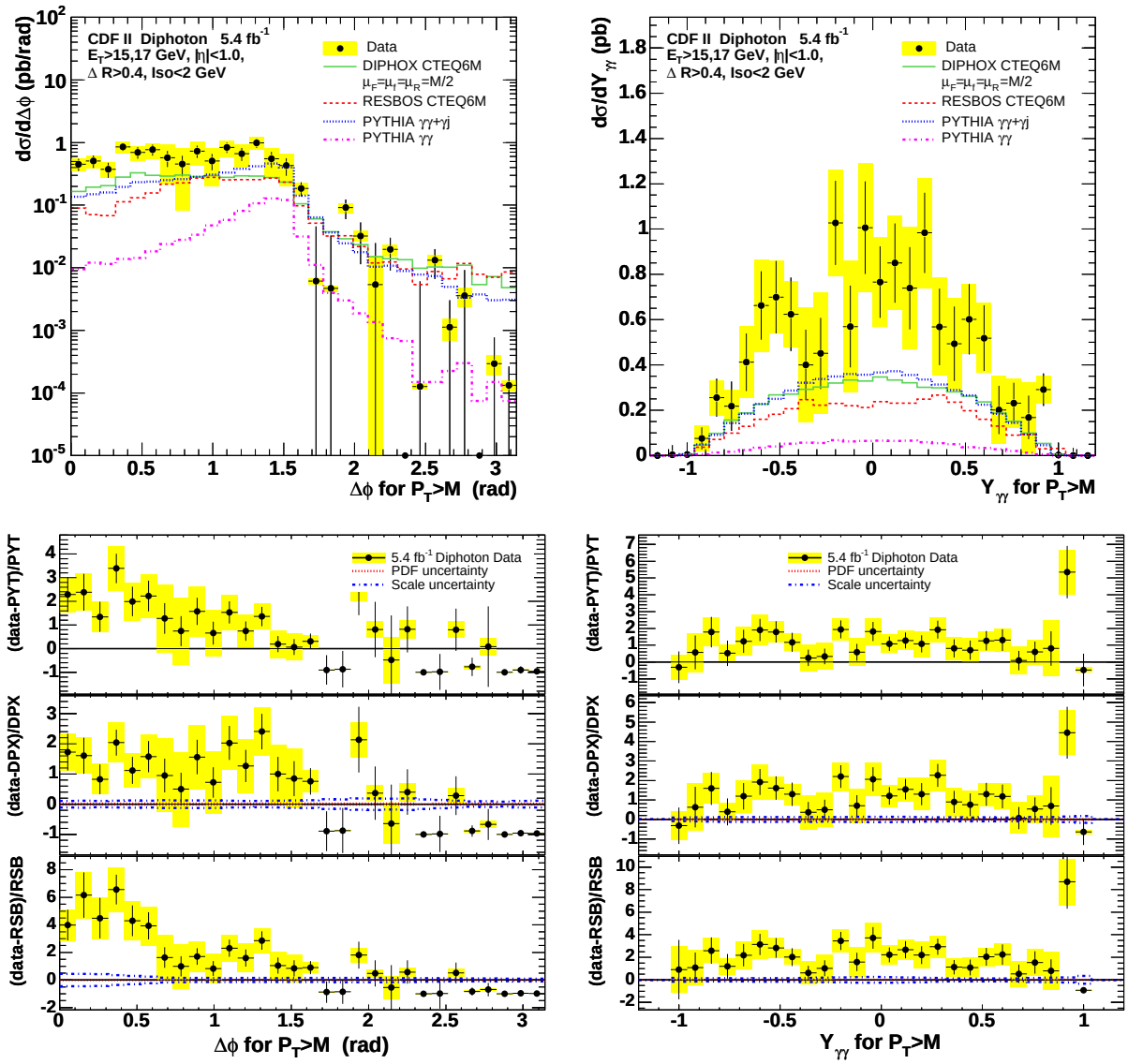

FIG. 20: The cross section as a function of the diphoton azimuthal distance (left) and of the diphoton rapidity (right) for $P_{\rm T}>M$. **Top:** the absolute cross section values. **Bottom:** the relative deviations of the data from the predictions. *Note:* the vertical axes scales differ between relative deviation plots. The shaded area is the total systematic uncertainty in the data.

vak R&D Agency; the Academy of Finland; and the Australian Research Council (ARC).

Appendix A: Content likelihood of the data sample

The signal and background disentanglement is done in a maximum likelihood framework. A likelihood of the composition of the baseline $\gamma\gamma$ sample is defined on the basis of binomial probabilities for the observed photons to pass or fail the track isolation cut:

$$\mathcal{L} = \prod_{ik} \mu_i(k)^{n_i(k)} [1 - \mu_i(k)]^{1-n_i(k)} \qquad \text{(A1)}$$

where $k = 1, \ldots, N$ labels all events in the sample and $i = pp, pf, fp, ff$ labels the categories of events in which both photons pass, the leading passes and the sub-leading fails, the leading fails and the sub-leading passes, and both photons fail the track isolation cut, respectively. $\mu_i(k)$ is the probability of the event k to fall in the category i and $n_i(k)$ is the observation for the event k; i.e. $n_i(k)$ is 1 for one of the four categories i and 0 for the other three. The probabilities can be analyzed as follows:

$$\mu_i(k) = \sum_j \varepsilon_{ij}(k) p_j(k) \qquad \text{(A2)}$$

where $j = ss, sb, bs, bb$ labels the categories in which both

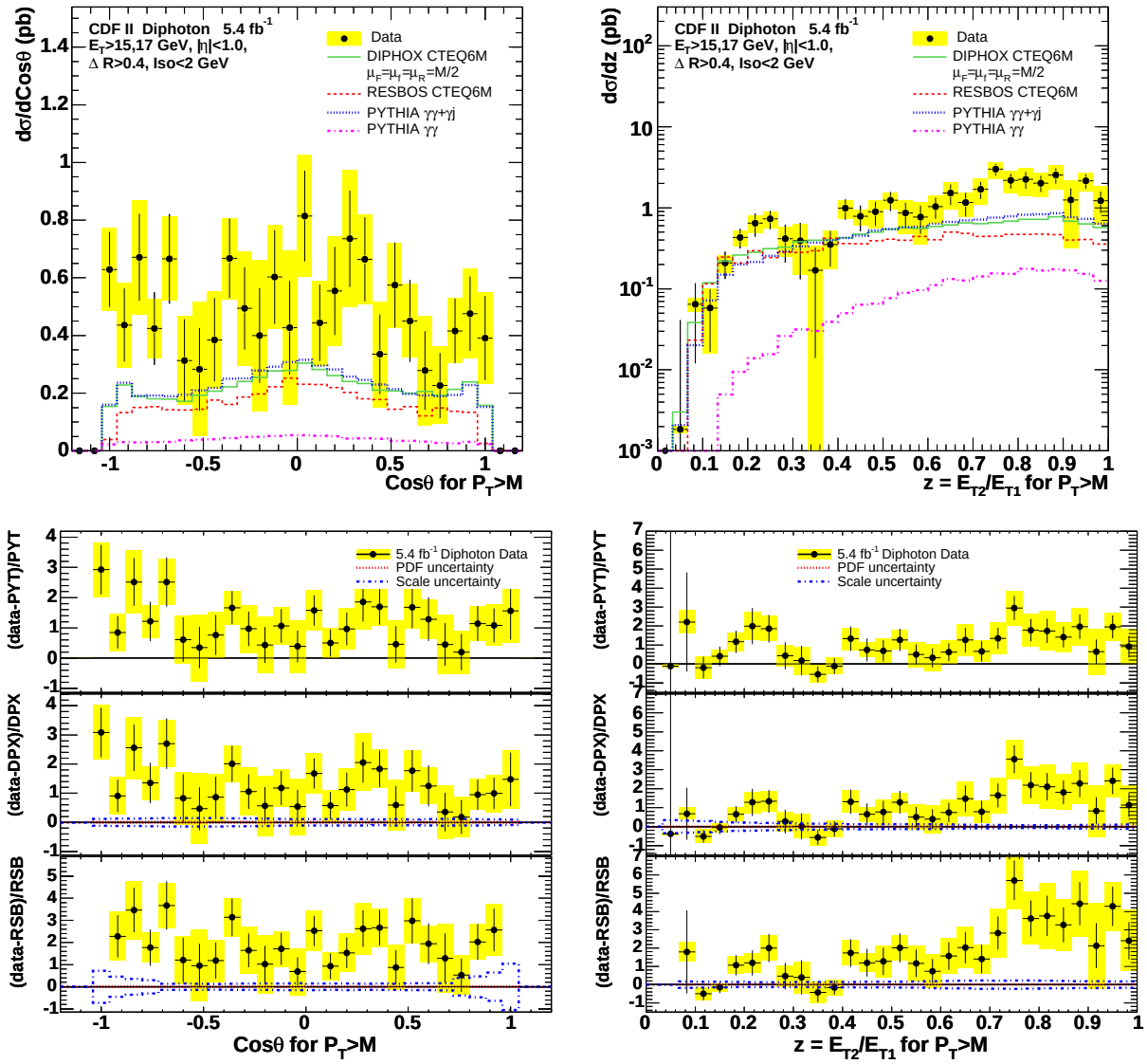

FIG. 21: The cross section as a function of the cosine of the polar angle in the Collins-Soper frame (left) and of the ratio of the subleading photon $E_{\rm T}$ to leading photon $E_{\rm T}$ (right) for $P_{\rm T}>M$. **Top:** the absolute cross section values. **Bottom:** the relative deviations of the data from the predictions. *Note:* the vertical axes scales differ between relative deviation plots. The shaded area is the total systematic uncertainty in the data.

photons are signal, the leading is signal and the sub-leading background, the leading is background and the sub-leading signal, and both photons are background, respectively. $p_j(k)$ is the probability for an event k to be in the category j. $\varepsilon_{ij}(k)$ is the probability for an event k of the truth category j to be observed in the observation category i. This probability is directly related with the efficiencies of the two photons in the event k to pass the track isolation cut, since the efficiencies are defined as the probabilities for the leading or sub-leading photon to pass the cut. In a 4×4 matrix notation,

$$\varepsilon(k) = \begin{pmatrix} \epsilon_{s1}(k)\epsilon_{s2}(k) & \epsilon_{s1}(k)\epsilon_{b2}(k) & \epsilon_{b1}(k)\epsilon_{s2}(k) & \epsilon_{b1}(k)\epsilon_{b2}(k) \\ \epsilon_{s1}(k)(1-\epsilon_{s2}(k)) & \epsilon_{s1}(k)(1-\epsilon_{b2}(k)) & \epsilon_{b1}(k)(1-\epsilon_{s2}(k)) & \epsilon_{b1}(k)(1-\epsilon_{b2}(k)) \\ (1-\epsilon_{s1}(k))\epsilon_{s2}(k) & (1-\epsilon_{s1}(k))\epsilon_{b2}(k) & (1-\epsilon_{b1}(k))\epsilon_{s2}(k) & (1-\epsilon_{b1}(k))\epsilon_{b2}(k) \\ (1-\epsilon_{s1}(k))(1-\epsilon_{s2}(k)) & (1-\epsilon_{s1}(k))(1-\epsilon_{b2}(k)) & (1-\epsilon_{b1}(k))(1-\epsilon_{s2}(k)) & (1-\epsilon_{b1}(k))(1-\epsilon_{b2}(k)) \end{pmatrix} \quad \text{(A3)}$$

where $\epsilon_{\alpha\beta}(k)$ ($\alpha = s$ or b, $\beta = 1$ or 2) are the efficiencies of the leading or sub-leading photon, coming from the signal or from the background, to pass the track isolation cut.

The likelihood $\mathcal{L}$ is maximized or, equivalently, the opposite of its natural logarithm

$$\begin{aligned} L &= -\ln \mathcal{L} \qquad \text{(A4)} \\ &= \sum_{ik} \left\{ n_i(k) \ln \mu_i(k) + [1 - n_i(k)] \ln [1 - \mu_i(k)] \right\} \end{aligned}$$

is minimized with respect to the probabilities $p_j(k)$. The minimization of the logarithm L leads to the system of equations

$$n_i(k) = \mu_i(k) = \sum_j \varepsilon_{ij}(k) p_j(k) \qquad \text{(A5)}$$

with solutions

$$p_j(k) = \sum_i \varepsilon^{-1}_{ji}(k) n_i(k) \qquad \text{(A6)}$$

The choice of the track isolation cut at 1 GeV/c gives the efficiencies $\epsilon_{\alpha\beta}(k)$ sufficient discriminating power among the truth categories j for the matrix $\varepsilon(k)$ to be non-singular. By summing the probabilties over all events in the baseline sample the maximum likelihood composition of the sample is obtained:

$$w_j = \sum_k p_j(k) = \sum_{ik} \varepsilon^{-1}_{ji}(k) n_i(k) \qquad \text{(A7)}$$

Eq. A7 for the truth category $j = ss$ provides the signal fraction in the baseline $\gamma\gamma$ sample.

In general, the composition of a sample of events with m photons each can be resolved in a maximum likelihood framework by the inversion of a $2^m \times 2^m$ matrix, constructed as in Eq. A3, which transforms the probability 2^m-vectors $p_j(k)$ to the observation 2^m-vectors $n_i(k)$. The generic matrix element $\varepsilon_{ij}(k)$ contains a factor $\epsilon_{\alpha\beta}(k)$ or $1 - \epsilon_{\alpha\beta}(k)$ for each photon $\beta = 1, 2, \ldots, m$ with $\alpha = s$ (b) if the photon is signal (background) in the truth category j and passes or fails, respectively, the track isolation cut in the observation category i. In this context, Eq. 1 for the single photon sample is derived from Eq. A7 by inverting for each event the matrix

$$\varepsilon = \begin{pmatrix} \epsilon_s & \epsilon_b \\ 1 - \epsilon_s & 1 - \epsilon_b \end{pmatrix}$$

$$\Rightarrow \varepsilon^{-1} = \frac{1}{\epsilon_s - \epsilon_b} \begin{pmatrix} 1 - \epsilon_b & -\epsilon_b \\ -1 + \epsilon_s & \epsilon_s \end{pmatrix} \qquad \text{(A8)}$$

with observation vectors

$$n_p = \begin{pmatrix} 1 \\ 0 \end{pmatrix} \qquad n_f = \begin{pmatrix} 0 \\ 1 \end{pmatrix} \qquad \text{(A9)}$$

for photons passing (n_p) or failing (n_f) the track isolation cut. Eq. A7 then gives for the signal fraction of the single photon sample

$$\begin{aligned} w_s &= \sum_p \left(\frac{1 - \epsilon_b}{\epsilon_s - \epsilon_b} \right)_p + \sum_f \left(\frac{-\epsilon_b}{\epsilon_s - \epsilon_b} \right)_f \\ &= \sum_i \left(\frac{\epsilon - \epsilon_b}{\epsilon_s - \epsilon_b} \right)_i \qquad \text{(A10)} \end{aligned}$$

where, in the first line, the first sum runs over all photons passing the cut and the second sum runs over all photons failing the cut. Eq. A10 is identical with Eq. 1.

Appendix B: Cross Section Tables

This Appendix provides a set of Tables of the measured differential cross section values as functions of the six kinematic variables selected in this analysis. Each Table lists the bins of the selected variable, the values of the cross section in the respective bins for the three examined cases of no kinematic cut, $P_{\mathrm{T}}<M$, and $P_{\mathrm{T}}>M$, and the statistical and total systematic uncertainties associated with each cross section value.

[1] T. Aaltonen *et al.* (CDF Collaboration), Phys. Rev. Lett. **103**, 061803 (2009); V. M. Abazov *et al.* (D0 Collaboration), Phys. Rev. Lett. **102**, 231801 (2009); G. Aad *et al.* (ATLAS Collaboration), arXiv:0901.0512 [hep-ex] (2009); G. L. Bayatian *et al.* (CMS Collaboration), J. Phys. G **34**, 995 (2007).

[2] T. Aaltonen *et al.* (CDF Collaboration), Phys. Rev. Lett. **99**, 171801 (2007); T. Aaltonen *et al.* (CDF Collaboration), Phys. Rev. D **83**, 011102 (2011); The CMS Collaboration, J. High Energy Phys. 05 (2011) 085; The ATLAS Collaboration, arXiv:1107.0561v2 [hep-ex] (2011).

[3] T. Sjöstrand, Comput. Phys. Commun. **82**, 74 (1994); S. Mrenna, Comput. Phys. Commun. **101**, 232 (1997).

[4] G. Corcella, I. G. Knowles, G. Marchesini, S. Moretti, K. Odagiri, P. Richardson, M. H. Seymour and B. R. Webber, J. High Energy Phys. 01 (2001) 010.

[5] S. Höche, S. Schumann and F. Siegert, Phys. Rev. **D81**, 034026 (2010).

TABLE V: The diphoton production cross section differential in the diphoton invariant mass. The first error in the cross section is statistical and the second systematic.

Mass bin [GeV/c^2]	Cross section without cut [pb/(GeV/c^2)]	Cross section for $P_{\rm T}<M$ [pb/(GeV/c^2)]	Cross section for $P_{\rm T}>M$ [pb/(GeV/c^2)]
0 - 5	0	0	0
5 - 10	$0.014679 \pm 0.002997 \pm 0.003369$	0	$0.014679 \pm 0.002997 \pm 0.003301$
10 - 15	$0.004441 \pm 0.000607 \pm 0.001115$	0	$0.036310 \pm 0.004965 \pm 0.009118$
15 - 20	$0.027568 \pm 0.005232 \pm 0.010986$	0	$0.029520 \pm 0.005602 \pm 0.011764$
20 - 25	$0.037459 \pm 0.005482 \pm 0.012486$	$0.000872 \pm 0.000686 \pm 0.000253$	$0.039767 \pm 0.005921 \pm 0.013317$
25 - 30	$0.046105 \pm 0.006060 \pm 0.016932$	$0.017214 \pm 0.004129 \pm 0.007523$	$0.008772 \pm 0.001367 \pm 0.002915$
30 - 35	$0.263727 \pm 0.014488 \pm 0.072680$	$0.242540 \pm 0.013891 \pm 0.066111$	$0.016857 \pm 0.003275 \pm 0.005552$
35 - 40	$0.515524 \pm 0.020876 \pm 0.153195$	$0.509522 \pm 0.021070 \pm 0.152077$	$0.012408 \pm 0.002360 \pm 0.003196$
40 - 45	$0.478042 \pm 0.018964 \pm 0.128524$	$0.467038 \pm 0.018734 \pm 0.125451$	$0.007605 \pm 0.002024 \pm 0.002203$
45 - 50	$0.322442 \pm 0.015234 \pm 0.088299$	$0.316623 \pm 0.015079 \pm 0.086365$	$0.003078 \pm 0.001149 \pm 0.001156$
50 - 55	$0.207378 \pm 0.011824 \pm 0.057932$	$0.201493 \pm 0.011730 \pm 0.056897$	$0.005372 \pm 0.001299 \pm 0.001027$
55 - 60	$0.134243 \pm 0.009249 \pm 0.036287$	$0.131094 \pm 0.009184 \pm 0.035695$	$0.003014 \pm 0.001053 \pm 0.000599$
60 - 65	$0.092296 \pm 0.007243 \pm 0.023721$	$0.089557 \pm 0.007169 \pm 0.023207$	$0.002944 \pm 0.001071 \pm 0.000583$
65 - 70	$0.064259 \pm 0.006117 \pm 0.017943$	$0.062955 \pm 0.006080 \pm 0.017584$	$0.001183 \pm 0.000629 \pm 0.000328$
70 - 75	$0.049211 \pm 0.005194 \pm 0.013341$	$0.047523 \pm 0.005150 \pm 0.012995$	$0.000942 \pm 0.000396 \pm 0.000201$
75 - 80	$0.042325 \pm 0.004477 \pm 0.009863$	$0.041887 \pm 0.004449 \pm 0.009750$	$0.000480 \pm 0.000536 \pm 0.000126$
80 - 85	$0.033129 \pm 0.003469 \pm 0.006708$	$0.032194 \pm 0.003436 \pm 0.006571$	$0.000875 \pm 0.000443 \pm 0.000173$
85 - 90	$0.024546 \pm 0.003230 \pm 0.005261$	$0.024111 \pm 0.003194 \pm 0.005127$	$0.000522 \pm 0.000577 \pm 0.000253$
90 - 95	$0.016972 \pm 0.002675 \pm 0.004167$	$0.016494 \pm 0.002657 \pm 0.004121$	$0.000286 \pm 0.000191 \pm 0.000056$
95 - 100	$0.016820 \pm 0.002418 \pm 0.003531$	$0.016531 \pm 0.002401 \pm 0.003486$	$0.000402 \pm 0.000405 \pm 0.000122$
100 - 110	$0.011975 \pm 0.001421 \pm 0.002450$	$0.011521 \pm 0.001407 \pm 0.002387$	$0.000272 \pm 0.000118 \pm 0.000047$
110 - 120	$0.009187 \pm 0.001193 \pm 0.001782$	$0.009037 \pm 0.001182 \pm 0.001747$	$0.000145 \pm 0.000156 \pm 0.000037$
120 - 130	$0.006673 \pm 0.000968 \pm 0.001262$	$0.006259 \pm 0.000953 \pm 0.001207$	$0.000292 \pm 0.000119 \pm 0.000071$
130 - 140	$0.005805 \pm 0.000856 \pm 0.001031$	$0.005742 \pm 0.000848 \pm 0.001017$	$0.000065 \pm 0.000109 \pm 0.000029$
140 - 160	$0.003414 \pm 0.000448 \pm 0.000602$	$0.003393 \pm 0.000444 \pm 0.000596$	$0.000027 \pm 0.000072 \pm 0.000018$
160 - 200	$0.001801 \pm 0.000208 \pm 0.000303$	$0.001757 \pm 0.000206 \pm 0.000296$	$0.000015 \pm 0.000009 \pm 0.000002$
200 - 250	$0.000573 \pm 0.000107 \pm 0.000101$	$0.000575 \pm 0.000107 \pm 0.000101$	0
250 - 300	$0.000182 \pm 0.000055 \pm 0.000030$	$0.000182 \pm 0.000055 \pm 0.000030$	0
300 - 350	$0.000207 \pm 0.000055 \pm 0.000035$	$0.000207 \pm 0.000055 \pm 0.000036$	0
350 - 500	$0.000064 \pm 0.000017 \pm 0.000011$	$0.000064 \pm 0.000017 \pm 0.000011$	0

[6] T. Binoth, J. P. Guillet, E. Pilon and M. Werlen, Eur. Phys. J. **C16**, 311 (2000); T. Binoth, J. P. Guillet, E. Pilon and M. Werlen, Phys. Rev. **D63**, 114016 (2001).

[7] Z. Bern, L. Dixon and C. Schmidt, Phys. Rev. **D66**, 074018 (2002).

[8] C. Balazs, E. L. Berger, P. Nadolsky and C.-P. Yuan, Phys. Lett. **D637**, 235 (2006); C. Balazs, E. L. Berger, P. Nadolsky and C.-P. Yuan, Phys. Rev. **D76**, 013009 (2007); C. Balazs, E. L. Berger, P. Nadolsky and C.-P. Yuan, Phys. Rev. **D76**, 013008 (2007).

[9] L. Bourhis, M. Fontannaz and J. P. Guillet, Eur. Phys. J. **C2**, 529 (1998).

[10] D. Acosta *et al.* (CDF Collaboration), Phys. Rev. Lett. **95**, 022003 (2005).

[11] V. M. Abazov *et al.* (D0 Collaboration), Phys. Lett. B **690**, 108 (2010).

[12] The CDF II detector uses a cylindrical coordinate system in which ϕ is the azimuthal angle, θ is the polar angle with respect to the proton beam, r is the radius from the nominal beam line, and z points in the proton beam direction, with the origin at the center of the detector. The transverse r-ϕ, or x-y plane, is the plane perpendicular to the z axis. The pseudorapidity, η, is defined as $-\ln(\tan(\theta/2))$. For the photons, which have zero mass, this is identical to the rapidity y=$\tanh^{-1}(p_{\rm z}/E)$, where $p_{\rm z}$=$p\cdot\cos\theta$ is the momentum parallel to the beam [30]. The transverse energy of a particle is $E_{\rm T}$=$E\cdot\sin\theta$. The transverse momentum of a particle is defined as $p_{\rm T}$=$p\cdot\sin\theta$.

[13] D. Acosta *et al.* (CDF Collaboration), Phys. Rev. D **71**, 032001 (2005).

[14] C.S. Hill *et al.*, Nucl. Instrum. Methods Phys. Res., Sect. A **511**, 118 (2003).

[15] A. Sill *et al.*, Nucl. Instrum. Methods Phys. Res., Sect. A **447**, 1 (2000).

[16] A. Affolder *et al.* (CDF Collaboration), Nucl. Instrum. Methods Phys. Res., Sect. A **453**, 84 (2000).

[17] A. Affolder *et al.* (CDF Collaboration), Nucl. Instrum. Methods Phys. Res., Sect. A **526**, 249 (2004).

[18] L. Balka *et al.*, Nucl. Instrum. Methods Phys. Res., Sect. A **267**, 272 (1988); S.R. Hahn *et al.*, *ibid.* **267**, 351 (1988).

[19] S. Bertolucci *et al.*, Nucl. Instrum. Methods Phys. Res., Sect. A **267**, 301 (1988).

[20] M. Goncharov *et al.*, Nucl. Instrum. Methods Phys. Res., Sect. A **565**, 543 (2006).

[21] D. Acosta *et al.*, Nucl. Instrum. Methods Phys. Res., Sect. A **494**, 57 (2002).

[22] F. Abe *et al.* (CDF Collaboration), Nucl. Instrum. Methods Phys. Res., Sect. A **271**, 387 (1988).

[23] For the central calorimeter, the fiducial region covers

TABLE VI: The diphoton production cross section differential in the diphoton transverse momentum. The first error in the cross section is statistical and the second systematic.

P_{T} bin [GeV/c]	Cross section without cut [pb/(GeV/c)]	Cross section for $P_{\mathrm{T}}<M$ [pb/(GeV/c)]	Cross section for $P_{\mathrm{T}}>M$ [pb/(GeV/c)]
0 - 1	$0.276549 \pm 0.030968 \pm 0.067613$	$0.276542 \pm 0.030967 \pm 0.067612$	0
1 - 2	$0.823081 \pm 0.051902 \pm 0.184444$	$0.823132 \pm 0.051905 \pm 0.184456$	0
2 - 3	$1.043320 \pm 0.056713 \pm 0.236673$	$1.043373 \pm 0.056716 \pm 0.236685$	0
3 - 4	$1.026369 \pm 0.055895 \pm 0.241145$	$1.026574 \pm 0.055907 \pm 0.241193$	0
4 - 5	$0.913944 \pm 0.055127 \pm 0.234272$	$0.914185 \pm 0.055142 \pm 0.234334$	0
5 - 6	$0.908628 \pm 0.053530 \pm 0.215222$	$0.909148 \pm 0.053560 \pm 0.215345$	0
6 - 7	$0.784121 \pm 0.049343 \pm 0.200779$	$0.784624 \pm 0.049375 \pm 0.200908$	0
7 - 8	$0.606111 \pm 0.045730 \pm 0.166151$	$0.606435 \pm 0.045755 \pm 0.166240$	0
8 - 9	$0.538172 \pm 0.042695 \pm 0.159898$	$0.538651 \pm 0.042733 \pm 0.160040$	0
9 - 10	$0.416951 \pm 0.039170 \pm 0.125580$	$0.417071 \pm 0.039181 \pm 0.125616$	0
10 - 12	$0.371872 \pm 0.025701 \pm 0.113307$	$0.372199 \pm 0.025723 \pm 0.113406$	0
12 - 14	$0.275282 \pm 0.022571 \pm 0.089464$	$0.275797 \pm 0.022613 \pm 0.089631$	0
14 - 16	$0.196349 \pm 0.019572 \pm 0.072611$	$0.196591 \pm 0.019597 \pm 0.072700$	0
16 - 18	$0.179301 \pm 0.017290 \pm 0.060538$	$0.179549 \pm 0.017314 \pm 0.060622$	0
18 - 20	$0.125584 \pm 0.015368 \pm 0.045351$	$0.126581 \pm 0.015490 \pm 0.045711$	0
20 - 25	$0.127625 \pm 0.009118 \pm 0.038128$	$0.125027 \pm 0.009019 \pm 0.037597$	$0.001932 \pm 0.000883 \pm 0.000457$
25 - 30	$0.092613 \pm 0.007839 \pm 0.028973$	$0.078351 \pm 0.006931 \pm 0.024441$	$0.013751 \pm 0.003737 \pm 0.004417$
30 - 35	$0.087187 \pm 0.007329 \pm 0.027382$	$0.040507 \pm 0.004874 \pm 0.012880$	$0.049065 \pm 0.005765 \pm 0.015309$
35 - 40	$0.056515 \pm 0.006341 \pm 0.020793$	$0.024564 \pm 0.003619 \pm 0.007531$	$0.033546 \pm 0.005550 \pm 0.014138$
40 - 45	$0.039824 \pm 0.004995 \pm 0.012246$	$0.012094 \pm 0.002774 \pm 0.004861$	$0.030706 \pm 0.004582 \pm 0.008315$
45 - 50	$0.022650 \pm 0.003604 \pm 0.006110$	$0.010569 \pm 0.002027 \pm 0.002311$	$0.012983 \pm 0.003290 \pm 0.004252$
50 - 60	$0.018204 \pm 0.002042 \pm 0.004416$	$0.006578 \pm 0.001173 \pm 0.001669$	$0.012472 \pm 0.001798 \pm 0.002971$
60 - 70	$0.007542 \pm 0.001410 \pm 0.002019$	$0.003080 \pm 0.000766 \pm 0.000693$	$0.004862 \pm 0.001318 \pm 0.001481$
70 - 80	$0.005717 \pm 0.001043 \pm 0.001271$	$0.001773 \pm 0.000483 \pm 0.000331$	$0.004388 \pm 0.001044 \pm 0.001080$
80 - 90	$0.003467 \pm 0.000656 \pm 0.000676$	$0.000801 \pm 0.000292 \pm 0.000167$	$0.003387 \pm 0.000749 \pm 0.000642$
90 - 100	$0.001355 \pm 0.000487 \pm 0.000377$	$0.000079 \pm 0.000188 \pm 0.000103$	$0.001242 \pm 0.000433 \pm 0.000279$
100 - 120	$0.001057 \pm 0.000212 \pm 0.000281$	$0.000198 \pm 0.000097 \pm 0.000062$	$0.000972 \pm 0.000212 \pm 0.000239$
120 - 140	$0.000655 \pm 0.000228 \pm 0.000135$	$0.000059 \pm 0.000071 \pm 0.000017$	$0.000516 \pm 0.000188 \pm 0.000094$
140 - 160	$0.000287 \pm 0.000122 \pm 0.000051$	$0.000008 \pm 0.000030 \pm 0.000007$	$0.001222 \pm 0.000496 \pm 0.000227$
160 - 200	$0.000100 \pm 0.000047 \pm 0.000021$	0	$0.000227 \pm 0.000105 \pm 0.000039$

∼87% of the total area.

[24] T. Aaltonen *et al.* (CDF Collaboration), Phys. Rev. D **82**, 052005 (2010).

[25] E. Gerchtein and M. Paulini, CHEP-2003-TUMT005, arXiv:physics/0306031 (2003); the version of GEANT used for the detector simulation is 3.21, see the CERN Program Library Long Writeup W5013.

[26] T. Aaltonen *et al.* (CDF Collaboration), Phys. Rev D **77**, 092001 (2008); Phys. Rev. Lett. **102**, 232002 (2009).

[27] H. L. Lai, J. Huston, S. Kuhlmann, J. Morfin, F. Olness, J.F. Owens, J. Pumplin and W. K. Tung, Eur. Phys. J. C **12**, 375 (2000).

[28] R. Field and C. Group, arXiv:0510198 [hep-ph] (2005).

[29] T. Aaltonen *et al.* (CDF Collaboration), Phys. Rev. D **80**, 111106 (2009).

[30] W. M. Yao *et al.*, "Review of Particle Physics", J. Phys. G **33**, 2006.

[31] D. Acosta *et al.* (CDF Collaboration), Phys. Rev. Lett. **94**, 091803 (2005).

[32] J. Pumplin, D. R. Stump, J. Huston, H. L. Lai, P. Nadolsky and W. K. Tung, J. HEP **0207**, 012 (2002).

[33] J. C. Collins and D. E. Soper, Phys. Rev D **16**, 2219 (1977).

TABLE VII: The diphoton production cross section differential in the diphoton azimuthal difference. The first error in the cross section is statistical and the second systematic.

$\Delta\phi$ bin [radians]	Cross section without cut [pb/rad]	Cross section for $P_{\rm T}<M$ [pb/rad]	Cross section for $P_{\rm T}>M$ [pb/rad]
0.000 - 0.105	$0.456343 \pm 0.099393 \pm 0.099826$	$0.008959 \pm 0.006342 \pm 0.004135$	$0.455591 \pm 0.101696 \pm 0.101433$
0.105 - 0.209	$0.443854 \pm 0.103665 \pm 0.101738$	0	$0.506682 \pm 0.116125 \pm 0.114737$
0.209 - 0.314	$0.346811 \pm 0.090621 \pm 0.085583$	$0.000964 \pm 0.000683 \pm 0.000446$	$0.377053 \pm 0.101504 \pm 0.096562$
0.314 - 0.419	$0.805494 \pm 0.112525 \pm 0.174161$	$0.008695 \pm 0.006135 \pm 0.001692$	$0.835398 \pm 0.118774 \pm 0.181144$
0.419 - 0.524	$0.621352 \pm 0.134650 \pm 0.162677$	0	$0.668658 \pm 0.139966 \pm 0.168432$
0.524 - 0.628	$0.695012 \pm 0.138448 \pm 0.183259$	$0.007809 \pm 0.011151 \pm 0.001958$	$0.712287 \pm 0.143289 \pm 0.188042$
0.628 - 0.733	$0.553260 \pm 0.152492 \pm 0.264377$	$0.023257 \pm 0.020326 \pm 0.006509$	$0.528230 \pm 0.151279 \pm 0.258421$
0.733 - 0.838	$0.375583 \pm 0.144617 \pm 0.261528$	0	$0.433524 \pm 0.158014 \pm 0.270138$
0.838 - 0.942	$0.671584 \pm 0.143112 \pm 0.228641$	$0.029115 \pm 0.020067 \pm 0.010039$	$0.679242 \pm 0.151863 \pm 0.231038$
0.942 - 1.047	$0.522112 \pm 0.137889 \pm 0.219688$	$0.038178 \pm 0.018111 \pm 0.008311$	$0.496178 \pm 0.145545 \pm 0.230738$
1.047 - 1.152	$0.864793 \pm 0.144971 \pm 0.220201$	$0.087654 \pm 0.032029 \pm 0.018939$	$0.781381 \pm 0.145224 \pm 0.207021$
1.152 - 1.257	$0.798674 \pm 0.154962 \pm 0.224791$	$0.150640 \pm 0.043789 \pm 0.033689$	$0.638090 \pm 0.150851 \pm 0.210793$
1.257 - 1.361	$1.124851 \pm 0.168956 \pm 0.257447$	$0.188806 \pm 0.056573 \pm 0.044931$	$0.939944 \pm 0.162249 \pm 0.212925$
1.361 - 1.466	$0.639906 \pm 0.169993 \pm 0.284205$	$0.118937 \pm 0.079298 \pm 0.074899$	$0.527203 \pm 0.151112 \pm 0.210203$
1.466 - 1.571	$0.834419 \pm 0.171606 \pm 0.270175$	$0.421297 \pm 0.113865 \pm 0.107330$	$0.408768 \pm 0.128128 \pm 0.171398$
1.571 - 1.676	$1.250665 \pm 0.169418 \pm 0.311391$	$1.007357 \pm 0.159164 \pm 0.278003$	$0.230173 \pm 0.057530 \pm 0.047005$
1.676 - 1.780	$0.832275 \pm 0.186990 \pm 0.364452$	$0.826622 \pm 0.181796 \pm 0.334001$	$0.006883 \pm 0.044420 \pm 0.000755$
1.780 - 1.885	$1.001287 \pm 0.187680 \pm 0.340539$	$0.998464 \pm 0.185177 \pm 0.326921$	$0.004982 \pm 0.030035 \pm 0.000548$
1.885 - 1.990	$1.076470 \pm 0.209360 \pm 0.442750$	$0.985068 \pm 0.206856 \pm 0.435764$	$0.097539 \pm 0.033960 \pm 0.017947$
1.990 - 2.094	$1.667315 \pm 0.233681 \pm 0.501973$	$1.628501 \pm 0.232554 \pm 0.498599$	$0.030895 \pm 0.019985 \pm 0.005693$
2.094 - 2.199	$2.275603 \pm 0.257154 \pm 0.585295$	$2.271233 \pm 0.256406 \pm 0.580308$	$0.005091 \pm 0.018432 \pm 0.007031$
2.199 - 2.304	$1.982347 \pm 0.275434 \pm 0.703905$	$1.945552 \pm 0.274931 \pm 0.703233$	$0.021202 \pm 0.011392 \pm 0.004164$
2.304 - 2.409	$3.180244 \pm 0.298472 \pm 0.883152$	$3.185517 \pm 0.298001 \pm 0.878647$	0
2.409 - 2.513	$3.344205 \pm 0.354571 \pm 1.099021$	$3.345126 \pm 0.354498 \pm 1.097423$	$0.000142 \pm 0.006657 \pm 0.000016$
2.513 - 2.618	$4.913562 \pm 0.403046 \pm 1.447020$	$4.883607 \pm 0.402930 \pm 1.445024$	$0.010602 \pm 0.005301 \pm 0.001996$
2.618 - 2.723	$6.787434 \pm 0.476941 \pm 1.881799$	$6.788491 \pm 0.477385 \pm 1.881996$	$0.000988 \pm 0.001690 \pm 0.000302$
2.723 - 2.827	$9.949192 \pm 0.584235 \pm 2.773900$	$9.948025 \pm 0.584526 \pm 2.773673$	$0.001445 \pm 0.002278 \pm 0.000396$
2.827 - 2.932	$14.781949 \pm 0.694936 \pm 3.966263$	$14.791632 \pm 0.695391 \pm 3.968861$	0
2.932 - 3.037	$21.597660 \pm 0.861897 \pm 5.826928$	$21.602392 \pm 0.862322 \pm 5.828225$	$0.000218 \pm 0.000352 \pm 0.000061$
3.037 - 3.142	$33.827076 \pm 0.998489 \pm 8.203793$	$33.825920 \pm 0.998661 \pm 8.204532$	$0.000133 \pm 0.000133 \pm 0.000024$

TABLE VIII: The diphoton production cross section differential in the diphoton rapidity. The first error in the cross section is statistical and the second systematic.

Y_{gg} bin	Cross section without cut [pb]	Cross section for $P_{\mathrm{T}}<M$ [pb]	Cross section for $P_{\mathrm{T}}>M$ [pb]
−1.20 - −1.12	$0.047796 \pm 0.032826 \pm 0.014355$	$0.047253 \pm 0.027906 \pm 0.017471$	$0.000543 \pm 0.017286 \pm 0.000059$
−1.12 - −1.04	$0.357094 \pm 0.120949 \pm 0.102530$	$0.353126 \pm 0.113517 \pm 0.089113$	$0.003968 \pm 0.041744 \pm 0.000434$
−1.04 - −0.96	$0.187965 \pm 0.037254 \pm 0.047292$	$0.179976 \pm 0.034997 \pm 0.041721$	$0.004941 \pm 0.006801 \pm 0.004111$
−0.96 - −0.88	$1.216128 \pm 0.179918 \pm 0.350105$	$1.123226 \pm 0.169654 \pm 0.303864$	$0.087621 \pm 0.056102 \pm 0.049798$
−0.88 - −0.80	$2.934750 \pm 0.300535 \pm 0.734394$	$2.634538 \pm 0.284117 \pm 0.653983$	$0.284037 \pm 0.092706 \pm 0.076637$
−0.80 - −0.72	$3.523381 \pm 0.364743 \pm 1.002344$	$3.275366 \pm 0.344374 \pm 0.929432$	$0.243582 \pm 0.121183 \pm 0.071961$
−0.72 - −0.64	$4.727782 \pm 0.415361 \pm 1.224628$	$4.251420 \pm 0.388978 \pm 1.079371$	$0.442221 \pm 0.136633 \pm 0.142010$
−0.64 - −0.56	$5.043031 \pm 0.463117 \pm 1.552137$	$4.391841 \pm 0.437811 \pm 1.375512$	$0.704898 \pm 0.160548 \pm 0.190566$
−0.56 - −0.48	$6.849294 \pm 0.521381 \pm 1.783643$	$6.156165 \pm 0.496178 \pm 1.631273$	$0.704821 \pm 0.161752 \pm 0.160419$
−0.48 - −0.40	$7.515287 \pm 0.565874 \pm 1.957807$	$6.894050 \pm 0.542207 \pm 1.818195$	$0.612712 \pm 0.159704 \pm 0.141450$
−0.40 - −0.32	$7.432176 \pm 0.605607 \pm 2.230531$	$7.009432 \pm 0.582405 \pm 2.029948$	$0.387476 \pm 0.149935 \pm 0.191711$
−0.32 - −0.24	$9.473290 \pm 0.644927 \pm 2.438148$	$9.018377 \pm 0.624024 \pm 2.249574$	$0.448143 \pm 0.156451 \pm 0.207981$
−0.24 - −0.16	$9.171682 \pm 0.650452 \pm 2.482947$	$8.178396 \pm 0.625007 \pm 2.276978$	$1.030157 \pm 0.186527 \pm 0.232884$
−0.16 - −0.08	$10.391827 \pm 0.673024 \pm 2.604154$	$9.833859 \pm 0.649550 \pm 2.409783$	$0.581114 \pm 0.183635 \pm 0.235125$
−0.08 - 0	$10.685762 \pm 0.683909 \pm 2.779428$	$9.737009 \pm 0.655963 \pm 2.536669$	$1.011320 \pm 0.205173 \pm 0.258684$
0 - 0.08	$9.778326 \pm 0.680032 \pm 2.746355$	$8.910962 \pm 0.656693 \pm 2.541139$	$0.779653 \pm 0.160122 \pm 0.189297$
0.08 - 0.16	$10.245283 \pm 0.664715 \pm 2.572113$	$9.428201 \pm 0.642795 \pm 2.382707$	$0.844021 \pm 0.173754 \pm 0.196508$
0.16 - 0.24	$8.898950 \pm 0.650517 \pm 2.522506$	$8.174833 \pm 0.625682 \pm 2.299986$	$0.740208 \pm 0.181740 \pm 0.229029$
0.24 - 0.32	$9.873399 \pm 0.639878 \pm 2.378116$	$8.881087 \pm 0.614339 \pm 2.143591$	$0.980913 \pm 0.177119 \pm 0.232361$
0.32 - 0.40	$8.208516 \pm 0.599002 \pm 2.150160$	$7.608601 \pm 0.571739 \pm 1.962087$	$0.575259 \pm 0.170775 \pm 0.186692$
0.40 - 0.48	$8.310832 \pm 0.582531 \pm 2.114900$	$7.805289 \pm 0.557393 \pm 1.950114$	$0.489608 \pm 0.162967 \pm 0.168822$
0.48 - 0.56	$6.158322 \pm 0.525197 \pm 1.682342$	$5.551052 \pm 0.501466 \pm 1.536281$	$0.602316 \pm 0.155006 \pm 0.146833$
0.56 - 0.64	$5.764018 \pm 0.484449 \pm 1.615546$	$5.254852 \pm 0.463164 \pm 1.480387$	$0.515143 \pm 0.143704 \pm 0.136823$
0.64 - 0.72	$3.746496 \pm 0.413343 \pm 1.272077$	$3.516958 \pm 0.394670 \pm 1.144314$	$0.219857 \pm 0.116288 \pm 0.126414$
0.72 - 0.80	$2.638815 \pm 0.344297 \pm 0.937298$	$2.365470 \pm 0.327398 \pm 0.833140$	$0.236348 \pm 0.092090 \pm 0.090185$
0.80 - 0.88	$1.908901 \pm 0.278836 \pm 0.661709$	$1.745827 \pm 0.263054 \pm 0.558774$	$0.178584 \pm 0.101977 \pm 0.123069$
0.88 - 0.96	$1.342328 \pm 0.185391 \pm 0.348576$	$1.092484 \pm 0.174767 \pm 0.311890$	$0.266332 \pm 0.065150 \pm 0.055395$
0.96 - 1.04	$0.125836 \pm 0.034791 \pm 0.043927$	$0.121207 \pm 0.033430 \pm 0.042727$	$0.002452 \pm 0.004579 \pm 0.000700$
1.04 - 1.12	$0.251782 \pm 0.113387 \pm 0.068974$	$0.278853 \pm 0.108155 \pm 0.064602$	0
1.12 - 1.20	$0.001304 \pm 0.029359 \pm 0.000143$	$0.001304 \pm 0.029359 \pm 0.000143$	0

TABLE IX: The diphoton production cross section differential in the cosine of the polar angle in Collins-Soper frame. The first error in the cross section is statistical and the second systematic.

$\cos\theta$ bin	Cross section without cut [pb]	Cross section for $P_{\rm T}<M$ [pb]	Cross section for $P_{\rm T}>M$ [pb]
−1.20 - −1.12	0	0	0
−1.12 - −1.04	0	0	0
−1.04 - −0.96	0.696711 ± 0.146723 ± 0.155742	0.000604 ± 0.012602 ± 0.000066	0.679356 ± 0.141129 ± 0.153197
−0.96 - −0.88	0.593058 ± 0.160701 ± 0.183348	0.043900 ± 0.032514 ± 0.018749	0.534910 ± 0.155592 ± 0.157684
−0.88 - −0.80	0.901409 ± 0.165027 ± 0.221503	0.214033 ± 0.066821 ± 0.046916	0.679008 ± 0.152504 ± 0.179300
−0.80 - −0.72	0.964840 ± 0.155297 ± 0.234473	0.686284 ± 0.131504 ± 0.167953	0.394443 ± 0.116872 ± 0.094604
−0.72 - −0.64	2.322500 ± 0.330788 ± 0.674056	1.895647 ± 0.321399 ± 0.603007	0.702685 ± 0.163956 ± 0.152732
−0.64 - −0.56	3.911811 ± 0.353577 ± 0.984306	3.971193 ± 0.364919 ± 0.976839	0.308842 ± 0.140763 ± 0.123241
−0.56 - −0.48	4.225161 ± 0.385762 ± 1.118926	4.381881 ± 0.405094 ± 1.105399	0.225221 ± 0.114141 ± 0.141418
−0.48 - −0.40	5.878916 ± 0.500103 ± 1.841742	5.998004 ± 0.523626 ± 1.862583	0.328751 ± 0.123479 ± 0.118609
−0.40 - −0.32	8.447426 ± 0.558218 ± 2.115941	8.476556 ± 0.589264 ± 2.168045	0.611133 ± 0.126341 ± 0.129931
−0.32 - −0.24	8.006947 ± 0.563629 ± 2.281457	8.205863 ± 0.595600 ± 2.316283	0.424552 ± 0.122576 ± 0.141255
−0.24 - −0.16	9.621518 ± 0.610748 ± 2.601253	10.100368 ± 0.646808 ± 2.669680	0.352094 ± 0.144908 ± 0.177738
−0.16 - −0.08	11.031545 ± 0.647516 ± 3.074353	11.400319 ± 0.685597 ± 3.182760	0.544025 ± 0.146581 ± 0.146555
−0.08 - 0	11.701358 ± 0.652059 ± 3.229385	12.252276 ± 0.687876 ± 3.313652	0.409344 ± 0.154987 ± 0.199857
0 - 0.08	10.744885 ± 0.639661 ± 3.180184	10.786094 ± 0.672314 ± 3.242347	0.808290 ± 0.156327 ± 0.195042
0.08 - 0.16	10.215599 ± 0.620273 ± 2.867342	10.599528 ± 0.657294 ± 2.971375	0.475211 ± 0.141936 ± 0.137377
0.16 - 0.24	8.894859 ± 0.591847 ± 2.681245	9.066109 ± 0.621564 ± 2.735215	0.593223 ± 0.163517 ± 0.176269
0.24 - 0.32	8.996937 ± 0.573034 ± 2.308823	9.083449 ± 0.602347 ± 2.317747	0.814932 ± 0.184770 ± 0.227355
0.32 - 0.40	8.131862 ± 0.550158 ± 2.082427	8.160151 ± 0.578638 ± 2.111536	0.687574 ± 0.151101 ± 0.156505
0.40 - 0.48	7.136364 ± 0.535862 ± 1.790615	7.337457 ± 0.558791 ± 1.797939	0.363666 ± 0.150402 ± 0.157323
0.48 - 0.56	6.314780 ± 0.443943 ± 1.479071	6.414981 ± 0.468845 ± 1.498226	0.642568 ± 0.164994 ± 0.156587
0.56 - 0.64	4.206630 ± 0.370591 ± 1.022774	4.311754 ± 0.395680 ± 1.044270	0.438339 ± 0.137911 ± 0.112795
0.64 - 0.72	2.507368 ± 0.287244 ± 0.605107	2.372216 ± 0.277399 ± 0.544206	0.242620 ± 0.118928 ± 0.127240
0.72 - 0.80	0.723595 ± 0.163114 ± 0.254653	0.508954 ± 0.128116 ± 0.162397	0.253995 ± 0.126498 ± 0.118790
0.80 - 0.88	0.553629 ± 0.131739 ± 0.141735	0.117661 ± 0.060000 ± 0.032288	0.422761 ± 0.113453 ± 0.106068
0.88 - 0.96	0.486210 ± 0.125296 ± 0.141378	0.046081 ± 0.036977 ± 0.015266	0.420675 ± 0.114459 ± 0.120587
0.96 - 1.04	0.389773 ± 0.141480 ± 0.142265	0.014859 ± 0.023566 ± 0.010889	0.372354 ± 0.138736 ± 0.128626
1.04 - 1.12	0	0	0
1.12 - 1.20	0	0	0

TABLE X: The diphoton production cross section differential in the sub-leading to leading photon transverse momentum ratio. The first error in the cross section is statistical and the second systematic.

z bin	Cross section without cut [pb]	Cross section for $P_{\mathrm{T}}<M$ [pb]	Cross section for $P_{\mathrm{T}}>M$ [pb]
0 - 0.033	0	0	0
0.033 - 0.067	$0.001845 \pm 0.039308 \pm 0.000183$	0	$0.001845 \pm 0.039308 \pm 0.000183$
0.067 - 0.100	$0.064683 \pm 0.052631 \pm 0.011964$	0	$0.064683 \pm 0.052631 \pm 0.011541$
0.100 - 0.133	$0.040160 \pm 0.027228 \pm 0.018852$	$0.014680 \pm 0.032433 \pm 0.004628$	$0.059705 \pm 0.042528 \pm 0.042287$
0.133 - 0.167	$0.208681 \pm 0.066194 \pm 0.042837$	$0.011290 \pm 0.006518 \pm 0.002107$	$0.219178 \pm 0.080746 \pm 0.052940$
0.167 - 0.200	$0.581526 \pm 0.144204 \pm 0.158584$	$0.130976 \pm 0.080148 \pm 0.047058$	$0.421745 \pm 0.112886 \pm 0.095122$
0.200 - 0.233	$0.687775 \pm 0.179968 \pm 0.138709$	$0.220290 \pm 0.099866 \pm 0.041656$	$0.624676 \pm 0.198432 \pm 0.138087$
0.233 - 0.267	$0.882504 \pm 0.219745 \pm 0.200850$	$0.311307 \pm 0.158139 \pm 0.120736$	$0.662516 \pm 0.169350 \pm 0.152908$
0.267 - 0.300	$1.254394 \pm 0.290529 \pm 0.272821$	$0.891524 \pm 0.232063 \pm 0.173525$	$0.380905 \pm 0.188202 \pm 0.125645$
0.300 - 0.333	$0.742542 \pm 0.342084 \pm 0.399154$	$0.427234 \pm 0.266842 \pm 0.247371$	$0.362702 \pm 0.241421 \pm 0.173907$
0.333 - 0.367	$0.633573 \pm 0.347426 \pm 0.629057$	$0.465991 \pm 0.313708 \pm 0.505393$	$0.171920 \pm 0.157777 \pm 0.130833$
0.367 - 0.400	$2.120037 \pm 0.452224 \pm 0.852624$	$1.715373 \pm 0.410393 \pm 0.695311$	$0.360338 \pm 0.169736 \pm 0.140800$
0.400 - 0.433	$3.736916 \pm 0.590222 \pm 1.123369$	$2.770300 \pm 0.524436 \pm 0.913390$	$1.008748 \pm 0.280388 \pm 0.241464$
0.433 - 0.467	$3.631943 \pm 0.628078 \pm 1.112420$	$2.889061 \pm 0.570550 \pm 0.962623$	$0.784327 \pm 0.273687 \pm 0.172160$
0.467 - 0.500	$4.521544 \pm 0.752621 \pm 1.788419$	$3.644498 \pm 0.692765 \pm 1.516931$	$0.862816 \pm 0.286054 \pm 0.268761$
0.500 - 0.533	$4.504285 \pm 0.765007 \pm 2.208000$	$3.370450 \pm 0.701471 \pm 2.016244$	$1.208186 \pm 0.316267 \pm 0.270012$
0.533 - 0.567	$5.323637 \pm 0.834206 \pm 2.560178$	$4.458064 \pm 0.775756 \pm 2.247832$	$0.852710 \pm 0.299524 \pm 0.308661$
0.567 - 0.600	$7.041574 \pm 0.923763 \pm 2.652894$	$6.228433 \pm 0.870212 \pm 2.309346$	$0.758477 \pm 0.289013 \pm 0.321800$
0.600 - 0.633	$8.403337 \pm 1.002178 \pm 3.176046$	$7.326917 \pm 0.951026 \pm 2.835386$	$1.050768 \pm 0.308693 \pm 0.336094$
0.633 - 0.667	$10.720245 \pm 1.130024 \pm 3.698758$	$9.382812 \pm 1.061512 \pm 3.277018$	$1.561377 \pm 0.447592 \pm 0.490694$
0.667 - 0.700	$12.252908 \pm 1.215009 \pm 4.376297$	$11.087163 \pm 1.154250 \pm 4.032151$	$1.190425 \pm 0.387427 \pm 0.352079$
0.700 - 0.733	$16.415794 \pm 1.325045 \pm 5.439192$	$14.773602 \pm 1.265468 \pm 4.943280$	$1.709796 \pm 0.404441 \pm 0.516840$
0.733 - 0.767	$24.203773 \pm 1.475829 \pm 6.110600$	$21.437672 \pm 1.403616 \pm 5.494815$	$2.989357 \pm 0.484161 \pm 0.680585$
0.767 - 0.800	$25.442360 \pm 1.568095 \pm 6.926982$	$23.305996 \pm 1.500378 \pm 6.332095$	$2.170811 \pm 0.461754 \pm 0.605827$
0.800 - 0.833	$26.262505 \pm 1.639982 \pm 7.542237$	$24.221176 \pm 1.570060 \pm 6.897027$	$2.164903 \pm 0.503890 \pm 0.696416$
0.833 - 0.867	$33.239754 \pm 1.758692 \pm 8.786769$	$31.182541 \pm 1.696572 \pm 8.184977$	$2.019600 \pm 0.455356 \pm 0.595763$
0.867 - 0.900	$43.423592 \pm 1.926264 \pm 10.230121$	$41.122257 \pm 1.860713 \pm 9.587927$	$2.478693 \pm 0.538976 \pm 0.732571$
0.900 - 0.933	$41.876434 \pm 1.940630 \pm 9.835004$	$40.736725 \pm 1.885258 \pm 9.372191$	$1.262268 \pm 0.497901 \pm 0.732053$
0.933 - 0.967	$46.414635 \pm 2.069529 \pm 10.663040$	$44.152313 \pm 2.017412 \pm 10.112022$	$2.116757 \pm 0.431365 \pm 0.515146$
0.967 - 1.000	$43.381981 \pm 2.094066 \pm 10.489670$	$41.883457 \pm 2.042450 \pm 9.953175$	$1.217864 \pm 0.363204 \pm 0.483372$